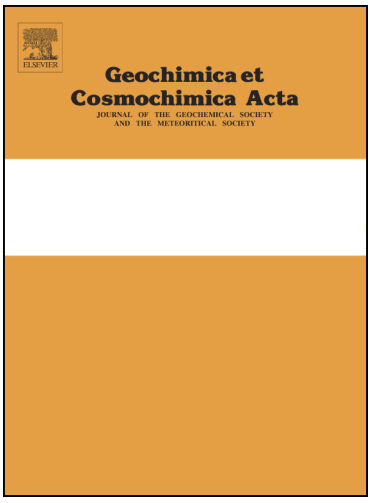

Effects of pH on redox proxies in a Jurassic rift lake: Implications for interpreting environmental records in deep time

Eva E. Stüeken, Aaron Martinez, Gordon Love, Paul E. Olsen, Steve Bates, Timothy W. Lyons

PII: S0016-7037(19)30152-8
DOI: https://doi.org/10.1016/j.gca.2019.03.014
Reference: GCA 11170

To appear in: *Geochimica et Cosmochimica Acta*

Received Date: 17 June 2018
Revised Date: 7 March 2019
Accepted Date: 7 March 2019

Please cite this article as: Stüeken, E.E., Martinez, A., Love, G., Olsen, P.E., Bates, S., Lyons, T.W., Effects of pH on redox proxies in a Jurassic rift lake: Implications for interpreting environmental records in deep time, *Geochimica et Cosmochimica Acta* (2019), doi: https://doi.org/10.1016/j.gca.2019.03.014

Effects of pH on redox proxies in a Jurassic rift lake: Implications for interpreting environmental records in deep time

Eva E. Stüeken[1,2,*], Aaron Martinez[3], Gordon Love[3], Paul E. Olsen[4], Steve Bates[3], Timothy W. Lyons[3]

1. University of St Andrews, School of Earth & Environmental Sciences, North Street, St Andrews, Fife, KY16 9AL, Scotland, UK
2. NASA Astrobiology Institute, Virtual Planetary Laboratory, University of Washington, Seattle, WA 98195, USA
3. University of California, Department of Earth Sciences, 900 University Avenue, Riverside, CA 92521, USA
4. Lamont-Doherty Earth Observatory of Columbia University, Department of Earth and Environmental Sciences, Palisades, NY 10964, USA
* corresponding author: ees4@st-andrews.ac.uk

Abstract

It is widely agreed that the Earth's atmosphere and oceans have undergone major redox changes over the last 2.5 billion years. However, the magnitude of these shifts remains a point of debate because it is difficult to reconstruct concentrations of dissolved O_2 from indirect proxies in sedimentary archives. In this study, we show that an additional complicating factor that is rarely considered may be the pH of the water column. We analyzed rock samples from the early Jurassic Towaco Formation in the Newark basin (eastern USA), comprising deposits of a rift lake that became temporarily redox stratified. New biomarker evidence points to increasingly saline aquatic conditions during the second half of the lake's history, with a salinity stratification that induced redox stratification, including evidence for water column anoxia, and that state may also explain the disappearance of macrofauna at this time. Distinctive lipid biomarker assemblages and stable nitrogen isotope data support previous mineralogical indications that the lake was alkaline (pH $\geq$ 9) during its saline episode. Despite the biomarker and macrofaunal evidence for anoxia, ratios of Fe/Al and Fe_{HR}/Fe_T show only small to no enrichments in the anoxic horizon compared to oxic facies in the same section – counter to what is commonly observed in anoxic marine settings. Molybdenum, As, V, U and to some degree Cd show enrichments in the anoxic interval, whereas Co, Ni, Cu, Zn and Cr do not. These patterns are most parsimoniously explained by differential pH effects on the solubility of these elements. Extrapolating from these observations in lacustrine strata, we speculate that a secular increase in seawater pH over Earth's history as recently proposed may have helped modulate the magnitude of trace metal enrichments in marine shales, although other factors such as atmospheric and oceanic redox likely dominated the observed enrichment patterns. Further, a decrease in the solubility of ferrous iron, a major O_2 sink, with increasing pH may have contributed to ocean oxygenation. In summary, our results highlight the potential importance of pH in influencing global biogeochemical cycles for multiple elements and for the interpretation of ancient nitrogen isotope signatures.

1. Introduction

Secular changes in the redox state of Earth's atmosphere and oceans have fundamentally impacted the evolution of biogeochemical cycles. For example, the Neoarchean-Paleoproterozoic rise of oxygen levels in terrestrial settings and in the atmosphere enhanced the release of sulfate into the ocean (Anbar et al., 2007; Kaufman et al., 2007; Reinhard et al., 2009; Stüeken et al., 2012; Kendall et al., 2015; Lalonde and Konhauser, 2015), which may help explain the transition from banded iron formations to pyritic black shale in shelf settings (e.g. Canfield, 1998; Scott et al., 2008; Poulton et al., 2010; Gilleaudeau and Kah, 2015; Partin et al., 2015; Cox et al., 2016). The establishment of oxic surface waters from that time onward (Kendall et al., 2015; Stüeken et al., 2015a; Hardisty et al., 2017; Kipp et al., 2017) allowed for the build-up of a nitrate reservoir in the surface ocean (Garvin et al., 2009; Godfrey and Falkowski, 2009; Busigny et al., 2013; Stüeken, 2013; Koehler et al., 2017; Zerkle et al., 2017). The Neoproterozoic rise of atmospheric oxygen was followed ultimately by the demise of anoxic deep waters in the Paleozoic and the build-up of redox-sensitive transition metals in seawater (Scott et al., 2008; Dahl et al., 2010; Och and Shields-Zhou, 2012; Sahoo et al., 2012; Chen et al., 2015; Sperling et al., 2015). Although oxygen imparted the first-order control on these transitions, it is conceivable that biogeochemical cycles have also been affected by other parameters, including pH. Recent model estimates suggest a gradual increase in seawater pH from ~6.5 in the Archean to modern values of > 8 (Halevy and Bachan, 2017; Isson and Planavsky, 2018), which may have influenced the mobility of major and minor elements. Importantly, in the range of pH 6-9, the solubility of ferrous iron in anoxic waters drops by more than an order of magnitude per one unit increase in pH (Morgan and Lahav, 2007), while molybdenum becomes more soluble, even in the presence of H_2S (Helz et al., 2011). Transition metal cations of Co, Ni, Cu and Zn behave like iron and show a decline in solubility with higher pH (Tack et al., 1996). We hypothesize that long-term changes in seawater pH as outlined by Halevy & Bachan (2017) could have contributed to the magnitude of enrichment in authigenic iron and other transition metals in marine sediments.

To test this hypothesis, we analyzed samples from the Early Jurassic Towaco Formation of the Newark Supergroup in the eastern U.S. As reviewed below, the Towaco Formation was deposited in a lacustrine setting with intermittent anoxic, high-pH (alkaline) intervals (Kruge et al., 1989; Pratt, 1989; Olsen et al., 1996a), comparable to other units in the Newark rift lakes

around this time (Van Houten, 1962; El Tabakh and Schreiber, 1994). This set of lacustrine rocks can thus serve as a natural laboratory to assess the effect of pH on biogeochemical proxies, including iron speciation and trace metal enrichments, even in marine settings.

2. Geologic setting

The Newark Supergroup in the eastern United States comprises a series of fluvial and lacustrine sedimentary rocks interbedded with basalt flows, in its younger parts, and intruded by diabase (diorite) sills and dikes (**Fig. 1**). The sediments were deposited in a series of half-grabens (**Fig. 2a**) that formed at tropical to subtropical latitudes during the early Mesozoic break-up of Pangaea prior to the opening of the central North Atlantic Ocean (e.g. Hay et al., 1982; Schlische, 1990; Witte et al., 1991; Kent and Tauxe, 2005). During the Triassic and extending into the Jurassic, regional climate was cycled quasi-periodically from relatively humid to arid conditions, with the end-members depending on paleolatitude (Olsen, 1986; Olsen and Kent, 1996; Kent and Tauxe, 2005). The Towaco Formation of the Newark Basin was deposited at approximately 21° N paleolatitude and experienced both arid and humid conditions. It is equivalent in age and comparable in lithostratigraphy to the East Berlin Formation in the Hartford Basin in Connecticut (Olsen, 2012). In the East Berlin Formation, previous studies inferred evaporitic conditions from the presence of occasional salts and abundant exposure surfaces, as well as carbon and oxygen isotopes in carbonates that point to evaporitic conditions (Suchecki et al., 1988, this study; El Tabakh and Schreiber, 1994). The humid phases are marked by the presence of very large and perennial lake sequences (Olsen, 1990). Overall, the setting may have been comparable to the modern East African rift lakes (Hay et al., 1982). Given the small paleogeographic separation between the Newark and Hartford basins and the similarities in age and depositional environment between the Towaco and East Berlin formations, it is conceivable that the two settings experienced similar conditions at this time, as will be tested in this study.

The sedimentary units in both basins include non-marine red beds, gray siltstones and black shales with variable amounts of carbonate. These lithologies show a striking cyclicity with recurrence intervals paced by Milankovitch cycles, indicating a strong climatic control on regional sedimentation rates, precipitation and even water chemistry (Olsen, 1986; Olsen and

Kent, 1996). The shortest and most notable cycle at outcrop scale is termed the Van Houten cycle (Olsen, 1986), with an inferred duration of ~20,000 years corresponding to the precession cycle (Olsen, 1986; Olsen and Kent, 1996; Whiteside et al., 2007; Blackburn et al., 2013). At our sampling locality, the stratigraphic thickness of Van Houten cycles is roughly 25 m (Olsen et al., 1996b). A typical Van Houten cycle within a perennial lake interval – as initially described by Van Houten (1965) and El Tabakh & Schreiber (1994) for other units in the Newark Basin – includes three divisions with varying thicknesses (**Fig. 2b**) (Olsen, 1986; Olsen and Kent, 1996) Moving up section from the base, these divisions comprise (i) a red to gray mudstone with progressively upward bed thinning and decreasing abundances of desiccation cracks, roots and/or burrows; (ii) planer-laminated shale, sometimes organic rich, with a basal horizon that is rich in fossils of fishes, crustaceans and sometimes reptiles; and (iii) another gray to red mudstone with a progressive decrease in the abundance of well-defined bedding and an increase of desiccation cracks and roots and burrows. Divisions 1 and 3 include evaporite pseudomorphs after Na-Ca sulfates (glauberite). All three divisions contain variable amounts of carbonate, including dolomite and calcite (Van Houten, 1965; Kruge et al., 1989; El Tabakh and Schreiber, 1994). In some Van Houten cycles in the Newark and Hartford basins, including portions of the East Berlin Formation that are time-equivalent to the Towaco Formation (Olsen, 2012), magnesite and analcime have been reported from the black shale facies (Van Houten, 1962; El Tabakh and Schreiber, 1994; Gierlowski-Kordesch and Rust, 1994), and authigenic albite has been reported from gray mudstones (Kruge et al., 1989).

Collectively, this sequence of lithologies and diagenetic minerals is interpreted as a climatically induced consequence of deepening and shallowing of an alkaline, sometimes saline lake, where the black shale facies (division 2) represents the high-stand interval (Olsen and Kent, 1996). The high abundance of organic matter (up to 8% in some cycles) and the absence of burrows in the deepest water facies likely indicate anoxic bottom waters (Kruge et al., 1989; El Tabakh and Schreiber, 1994; Olsen and Kent, 1996). During their deepest intervals, Newark lakes were probably chemically stratified.

We collected samples from two drill-cores (C-128 and PT-14, **Fig. 1**) through one Van Houten cycle (that containing the Colfax Bed, Olsen, 2011) of the early Jurassic Towaco Formation in the Newark basin (Olsen et al., 1996a; Weems and Olsen, 1997; Olsen, 2011). The Towaco Formation is approximately 350 m thick and bracketed by the Preakness Basalt and the

Hook Mountain Basalt (**Fig. 1**) (Schlische, 1990; Olsen et al., 1996a). This interval was chosen because it was easily accessible through relatively fresh drill-core and because of its relatively low thermal maturity (%R0 = 0.50, H/C ratios ~0.95, Tmax = 426°C, Hatcher and Romankiw, 1985; Pratt et al., 1985; Malinconico, 2002). Furthermore, this cycle contains a thin but distinctive ash bed – the Pompton Tuff (Olsen, 2012) – which allows us to correlate this unit with a Van Houten cycle in the East Berlin Formation in the Hartford basin, another rift lake of the Newark Supergroup. Previous studies of the Hartford basin have reported magnesite ($MgCO_3$) and organic biomarkers indicative of moderately saline and alkaline conditions (Kruge et al., 1989; Gierlowski-Kordesch and Rust, 1994). These biomarkers include carotanes and extended tricyclic terpanes, which are commonly found in saline environments, including alkaline lakes (De Grande et al., 1993), although they are not indicative of saline conditions on their own. Carotanes have previously been reported from analyses of the Towaco Formation (Kruge et al., 1989; Pratt, 1989). Lastly, a past study of the carbon isotope composition and aromaticity of the black shales in the Towaco Formation suggested a high percentage (60-90%) of algal biomass, with relatively small contributions of detrital plant material (Spiker et al., 1988), which should allow us to isolate biogeochemical processes specific to the local water column.

3. Analytical methods

3.1. Sample preparation

Sample preparation and analyses followed standard protocols. The outer surfaces of the core samples were removed with a water-cooled rock saw. The samples were then hammered into sub-cm sized chips, which were transferred into an acid-washed glass beaker and sonicated for a few seconds in 2M HCl. The acid was removed during multiple rinses with DI-H_2O (18 MΩ) in the sonic bath. The clean rock ships were air-dried in loosely covered plastic weigh boats and then pulverized to a fine powder in a ball mill. The powders were stored in acid-washed plastic vials.

3.2. Total nitrogen and organic carbon

Sample preparation and analyses of carbon and nitrogen isotopes were carried out at the University of Washington. A ~0.5 g aliquot of each powder was weighed into a glass centrifuge tube and decarbonated with 6M HCl at 60°C overnight (Stüeken et al., 2015b; Stüeken et al., 2015c). The acid was refreshed twice and stirred with a glass rod. The powders were then washed three times with DI-H_2O (18 MΩ) and dried for three days in an oven at 60°C. For analyses of total organic carbon (TOC), total nitrogen (TN), organic carbon isotopes and total nitrogen isotopes, the dry powders were weighed into 9 x 5 mm tin capsules and analyzed by flash combustion with an Costech EA coupled via a Conflo III to Thermo Finnigan MAT253 IRMS. The average reproducibility of samples was 0.25‰ for $\delta^{15}N_{bulk}$ (1 standard deviation, SD), 0.15‰ for $\delta^{13}C_{org}$ (1 SD), 0.5% for TOC (relative error, RE), 5% for TN (RE) and 5% for C/N ratios (RE). We obtained values of $\delta^{15}N_{bulk}$ = 5.37 ± 0.46‰, $\delta^{13}C_{org}$ = -37.84 ± 0.61‰, TOC = 7.4 ± 0.2% and TN = 1019 ± 96 ppm for our UW-McRae in-house standard, which agree well with previous studies (Stüeken et al., 2015b; Stüeken et al., 2015c). The isotopic data were expressed in delta notation relative to VPDB for $\delta^{13}C_{org}$ and relative to air for $\delta^{15}N$: δ [‰] = ($^{x/y}R_{sample}$ / $^{x/y}R_{standard}$ - 1), where $^{x/y}R$ = $^{15}N/^{14}N$ for nitrogen and $^{13}C/^{12}C$ for carbon.

3.3. Carbonate carbon and oxygen isotope data

Untreated powder aliquots were weighed into acid-washed glass vials and reacted with concentrated phosphoric acid at 80°C for 12 minutes in a Kiel III carbonate device (Stüeken, 2013). The resulting CO_2 was purified cryogenically and analyzed with a Thermo Finnigan Delta Plus IRMS. The reproducibility (1 SD) was 0.05‰ for $\delta^{13}C_{carb}$ and 0.13‰ for $\delta^{18}O_{carb}$. Our calibration standards were all calcite, which is known to experience a slightly different oxygen isotope fractionation during phosphoric acid dissolution compared to dolomite (Guo et al., 2009 and references therein). The difference is about 1‰ at 80°C for end-member mineralogies (Guo et al., 2009). As shown below (Section 4.3), our samples mostly contain dolomite. However, we did not apply a correction for this mineralogical effect because Mg/Ca ratios and hence the mineralogy show some variability in our samples, which makes it difficult to predict the exact magnitude of the effect. This observation does not compromise our interpretation because (i) the possible effect of 1‰ is relatively small compared to the 6‰ range in our $\delta^{18}O_{carb}$ data and (ii)

Mg/Ca ratios do not covary with oxygen isotope ratios ($r^2 = 0.19$), confirming that this analytical fractionation effect cannot explain the observed trends in $\delta^{18}O_{carb}$ discussed below. Both $\delta^{13}C_{carb}$ and $\delta^{18}O_{carb}$ data were expressed in delta notation relative to VPDB: δ [‰] = ($^{x/y}R_{sample}$ / $^{x/y}R_{standard}$ - 1), where $^{x/y}R = {}^{18}O/{}^{16}O$ for oxygen and $^{13}C/^{12}C$ for carbon.

3.4. Elemental abundances

Sample preparation and analyses of elemental abundances and iron speciation (Section 3.5) were carried out at the University of California, Riverside. Approximately 100 mg of untreated powder were weighed into ceramic crucibles and ashed overnight at 800°C (Reinhard et al., 2013). The powder was then transferred into a Teflon beaker and dissolved with 5 ml of concentrated HNO_3 and 1 ml of concentrated HF (both trace metal grade) at 130°C overnight (Reinhard et al., 2013). After evaporation at 110°C, secondary fluoride precipitates were dissolved with 4 ml of aqua regia (3:1 HNO_3 and HCl). The aqua regia treatment was repeated once. The samples were then evaporated to incipient dryness, re-dissolved in 5 ml of 5% HNO_3 (v/v) and stored in acid-washed Nalgene bottles. For elemental analyses, the samples were diluted 1:100 by mass with 2% HNO_3 and analyzed with an Agilent 7900 ICP-MS. Average reproducibility of samples was 10% (RE) or better for all elements. Average accuracy as monitored with the USGS standards SDo-1, SCo-1 and BCR-2 was 10% or better. Enrichment factors (EF) for trace metals (X) relative to crustal background were calculated as EF = (X [%]/Al [%])$_{sample}$ / (X [%]/Al [%])$_{crust}$, where crustal concentrations were approximated by the composition of red shales in the drill-cores. This local reference point allows us to interpret metal enrichments in sediments where the exact composition of source rocks is unknown. We note, however, that our interpretation would not change if we used average continental crust (Rudnick and Gao, 2014) as an anchor point for the calculation of enrichment factors.

3.5. Iron speciation

To extract iron bound in carbonate (Fe_{CARB}), ferric oxides (Fe_{HEM}) and magnetite (Fe_{MAG}) in this order, around 100 mg of powder were weighed into Falcon centrifuge tubes and treated sequentially with sodium acetate (1 M, 10 ml, buffered to pH 4.5 with acetic acid, 48 hours),

sodium dithionite (50 g/L, 10 ml, buffered to pH 4.8 with 0.35 M acetic acid and 0.2 M sodium citrate, 2 hours) and ammonium oxalate (0.2 M, 10 ml, buffered to pH 3.2 with 0.17 M NH_4OH, 6 hours) (Poulton and Canfield, 2005; Reinhard et al., 2009; Reinhard et al., 2013). After each treatment, the samples were centrifuged, and 4 ml of solution were extracted with a pipette for analysis. The remainder was discarded. The analyses were performed using an Agilent 7500 ICP-MS following the same procedure as for total digests (Section 3.4). Calcium and Mg concentrations in the acetic acid fraction were used to determine the relative abundances of $CaCO_3$ and $MgCO_3$ end members in the samples. The average reproducibility for the three iron fractions was between 5% and 20% (RE). Pyrite-bound sulfur was extracted using the chromium reduction method on a separate aliquot of powder. The samples were boiled with a mixture of concentrated HCl (15 ml) and 1M $CrCl_2$ (in 0.5 M HCl, 35 ml) under a constant stream of N_2 gas for two hours (Canfield et al., 1986; Reinhard et al., 2009; Reinhard et al., 2013). The H_2S generated during the reaction between pyrite and Cr^{2+} was captured with a solution of 3% Zn acetate in 10% NH_4OH. The pyrite-sulfur content was then measured by iodometric titration (Canfield et al., 1986). The reproducibility was between 5% and 15% (RE). We assumed a FeS_2 stoichiometry to calculate the pyrite-bound iron (Fe_{Py}) from the measured amount of pyrite sulfur. The sum of all four extracted iron phases (Fe_{CARB} + Fe_{HEM} + Fe_{MAG} + Fe_{PY}) is defined as the total amount of 'highly reactive' iron (Fe_{HR}) (Poulton and Canfield, 2005).

3.6. Pyrite sulfur isotopes

For sulfur isotope analyses, samples were prepared by chromium reduction as described above (Section 3.5). However, the H_2S gas was trapped with a solution of 3% $AgNO_3$ in 10% NH_4OH. The Ag_2S precipitate was dried at 45°C in a closed oven. Analyses were carried out at the University of Washington using a Eurovector EA coupled to a Thermo Finnigan MAT253 IRMS. The reproducibility was 1.2‰ (1 SD). Results are expressed in delta notation relative to VCDT: $\delta^{34}S\ [‰] = (^{34}S/^{32}S)_{sample}/(^{34}S/^{32}S)_{standard} - 1$.

3.7. Organic geochemistry

Crushed rock powders were extracted in a CEM Microwave Accelerated Reaction System (MARS) at 100°C in a 9:1 DCM:MeOH (v/v) mixture for 15 min to yield rock bitumens. Full laboratory procedural blanks with pre-combusted sand were performed in parallel to ensure that any background hydrocarbon compounds were negligible in comparison with biomarker analyte abundances. Saturated hydrocarbon and aromatic fractions were obtained by silica gel column chromatography, and the saturated hydrocarbon fractions were eluted with n-hexane and the aromatic hydrocarbon fractions with a 1:1 (v/v) mixture of DCM and n-hexane.

Saturated hydrocarbon fractions were analyzed by metastable reaction monitoring–gas chromatography–mass spectrometry (MRM-GC-MS) conducted at UC Riverside on a Waters AutoSpec Premier mass spectrometer equipped with a HP 6890 gas chromatograph and DB-1MS coated capillary column (60 m × 0.25 mm, 0.25 μm film thickness) using He as the carrier gas. The GC temperature program consisted of an initial hold at 60°C for 2 min, heating to 150°C at 10 °C/min followed by heating to 320°C at 3°C/min and a final hold for 22 min. Analyses were performed via splitless injection in electron impact mode, with an ionization energy of 70 eV and an accelerating voltage of 8 kV. MRM transitions for C_{27}–C_{35} hopanes, C_{31}–C_{36} methylhopanes, C_{21}–C_{22} and C_{26}–C_{30} steranes, C_{30} methylsteranes and C_{19}–C_{26} tricyclics were monitored. Polycyclic biomarker alkanes (tricyclic terpanes, hopanes, steranes, etc.) were quantified by addition of a deuterated C_{29} sterane standard (d4-ααα-24-ethylcholestane [20R]) to saturated hydrocarbon fractions and comparison of relative peak areas.

Saturated and aromatic hydrocarbon fractions were analyzed in both full scan and single ion monitoring methods at UC Riverside by gas chromatography–mass spectrometry (GC-MS) on an Agilent 7890A GC system coupled to an Agilent 5975C inert MSD mass spectrometer. The GC was equipped with a DB1-MS capillary column (60 m × 0.32 mm, 0.25 μm film thickness), and helium was used as the carrier gas. The temperature program for GC-MS full scan and selected ion monitoring was 60ºC (2 min hold), ramped to 150ºC at 20ºC/min, then to 325ºC at 2ºC/min and held at 325ºC for 20 min. C_{40} carotanes, including β-carotane, γ-carotane and their structural isomers, were identified in saturated hydrocarbon fractions based on 125 Dalton (Da) mass chromatograms and verified from mass spectra and retention time.

3.8. Petrography

Billets were cut for a subset of samples and submitted to National Petrographic for preparation of standard thin section. The thin sections were analyzed with optical microscopy using transmitted light.

4. Results

4.1. Sample description

The two drill cores, which transect the same stratigraphic unit, show matching lithofacies with similar thicknesses (**Fig. 3 and 4**) and thus will be presented in a single description. The sampled section can be broadly divided into five parts: (i) a lower red siltstone to silty shale; (ii) a lower greenish-gray mudstone, 2 m thick; (iii) a black shale, 1.5 m thick; (iv) an upper greenish-gray mudstone, 5 m thick and (v) an upper red siltstone to silty shale. Units (i) and (v) are mostly composed of interlaminated red shale and red siltstone with lenses of fine sandstone. Individual laminae are several mm thick and sometimes graded or wavy. Some coarser-grained laminae display cross-bedding, while the finer intervals – especially toward the base and top of the two drill core sections – show pedogenic features, including desiccation cracks and rare nodular carbonate. Units (ii) and (iv) are mostly composed of interbedded massive and bioturbated mudstones with weakly graded cm-scale silty shale interbeds. Bioturbation is most prevalent proximal to the red siltstone units. In unit (ii), the grain size generally decreases upward from silt- to clay-dominated, whereas unit (iv) shows a coarsening-upward trend. Finely disseminated pyrite is present throughout most of gray mudstone, in particular in unit (ii) (**Fig. 5**). Euhedral pyrite grains (up to ~0.1 mm) tend to be associated with mm-scale sparry carbonate fenestrae. Unit (iii) is composed of plane-to-wrinkly laminated dark brown to black shale (**Fig. 5**). Individual laminae are less than one mm thick and defined by varying contents of carbonate and organic matter. Pyrite is generally not visible with a hand lens or under the microscope in the black shale. The basal 10 cm of this bed is microlaminated and contains whole fish fossils and a distinct pyritic ash bed that is about 0.5 cm thick (the Pompton Tuff). This microlaminite horizon is traceable over many kilometers in the Towaco Formation (Olsen, 1988a). We only obtained small samples of this microlaminite from core C-128 (sampled at 0.5 cm scale), which was

sufficient for inorganic analyses but insufficient for biomarker work. The tuff bed is at 51.664 m depth (sample ID C128TUFF-4)

4.2. Organic carbon and nitrogen systematics

Total organic carbon (TOC) abundances show a distinct peak up to 6.6% in the 1-m-thick black shale horizon in both cores (**Fig. 3 and 4**, **Table 1**). This peak is established somewhat gradually over the lower 2 m of the gray mudstone, with intermediate values around 1%, but it ends comparatively abruptly with TOC values dropping down to < 0.5% in the upper gray mudstone. Total nitrogen is well correlated with organic carbon content in both cores ($r^2 = 0.91$), indicating that it is mostly organic-bound or derived from organic matter degradation. Ratios of organic carbon to total nitrogen (C/N) covary with TOC (**Fig. 6b**), meaning that samples with higher biomass tend to be relatively nitrogen-depleted. This trend levels off slightly above ~2% TOC (**Fig. 6b**) where the slope between C/N ratios and TOC becomes shallower.

Organic carbon isotopes ($\delta^{13}C_{org}$) range from -24‰ to -30‰, and the lighter values occur mostly within the lower gray mudstone and the black shale. Above the black shale, $\delta^{13}C_{org}$ is systematically heavier (**Fig. 3 and 4**). Samples with $\delta^{13}C_{org}$ > -29‰ all have < 0.5% TOC and vice versa (**Fig. 6d**). Total nitrogen isotope data ($\delta^{15}N_{bulk}$) range from 3‰ to 15‰, in good agreement with two previous measurements (Spiker, 1985). Values above 6‰ are restricted to the black shale horizon (**Fig. 3 and 4**), which is also the interval with the lowest $\delta^{13}C_{org}$ and the highest TOC and C/N values (**Fig. 6**). Given that this interval occurs in the middle of the section, it is unlikely that the correlation between $\delta^{15}N_{bulk}$ and C/N is a metamorphic feature (cf. Haendel et al., 1986).

4.3. Carbonate C-O isotopes and mineralogy

The carbonate content (**Table 1**) of the samples is around 5% or less in the lower red siltstone and gray mudstone. It then increases to a maximum of 58% in the black microlaminite and stays to around 30% in the rest of the black shale before dropping to intermediate values of 7-13% in the upper gray mudstone (**Fig. 3 and 4**). The upper red shale is again carbonate-poor (less than a few percent). Values for $\delta^{13}C_{carb}$ and $\delta^{18}O_{carb}$ broadly covary across the section (r^2 =

0.49 for all samples, and $r^2 = 0.68$ without the microlaminite; $\delta^{13}C_{carb}$ in the microlaminite might have been affected by organic matter remineralization). In the lower gray mudstone, the values fall mostly around -2‰ for $\delta^{13}C_{carb}$ and +0.5‰ for $\delta^{18}O_{carb}$. The first few samples in the basal part of the black shale horizon show a negative excursion down to -5‰ in $\delta^{13}C_{carb}$ (with one outlier of -11‰ immediately under the tuff bed, which may be due to combustion of organic carbon during tuff accumulation) and -4‰ in $\delta^{18}O_{carb}$. Both parameters then increase steeply up section to +0.8‰ ($\delta^{13}C_{carb}$) and +2.2‰ ($\delta^{18}O_{carb}$), respectively, and remain high in the upper part of the section. Molar Ca/Mg ratios in carbonates, as determined from the acetic acid extraction, show a geometric mean of 1.3 +0.8/-0.5 with a few outliers of up to 7.9 but with no systematic variance throughout the section, suggesting a uniformly dolomitic mineralogy.

4.4. Iron and sulfur systematics

Ratios of total iron to aluminum (Fe/Al) are nearly constant throughout the section (**Fig. 3 and 4**), including the black shale, with an overall mean of 0.57 ± 0.14 (2 SD). The tuff bed marks an outlier with an Fe/Al ratio of 1.4 due to the high abundance of pyrite (~14%, see below). Ratios of highly reactive to total iron (Fe_{HR}/Fe_T) vary between 0.32 and 0.52 in the lower and upper gray mudstone and the black shale above the microlaminite. Within the microlaminite in core C-128, Fe_{HR}/Fe_T ratios range from 0.57 to 0.8 with a peak at 1.0 in the tuff bed, but they then decline up section into the black shale horizon, from ~0.45 to 0.32, followed by a return to ~0.45. The red shales of both cores have mean Fe_{HR}/Fe_T ratios of 0.30 ± 0.18 (2 SD). These red, presumably oxic facies constrain the relative abundance of reactive iron phases in the siliciclastic background – that is, the local detrital input (Raiswell and Canfield, 1998). Hence, by comparison to the red shales, the black shale is only weakly enriched in Fe_{HR}/Fe_T (**Fig. 7a**).

Ratios of Fe_{PY}/Fe_{HR} (**Table 2**) are more variable than Fe_{HR}/Fe_T throughout the section. Within in the lower gray mudstone and extending into the first few meters of the upper gray mudstone, Fe_{PY}/Fe_{HR} increases steeply up section from 0 to 0.90 (**Fig. 3 and 4**). In the microlaminite and again in the middle of the black shale, Fe_{PY}/Fe_{HR} ratios show distinct drops to 0.50 and 0.45, respectively. The tuff bed marks an exception ($Fe_{PY}/Fe_{HR} = 0.84$) because it contains around 14% pyrite, likely related to volcanic emissions. In the upper gray mudstone, most of the reactive iron is bound to carbonate (Fe_{CARB}/Fe_{HR} up to 0.68) (**Fig. 8**). In the red

shales, reactive iron is dominated by ferric iron oxides (Fe_{HEM}/Fe_{HR} up to 0.84). Importantly, the transition from pyrite-bound iron to carbonate-bound iron does not coincide with an increase in carbonate abundance (**Fig. 3 and 4**), indicating that carbonate does not impart the first-order control on reactive iron trends. Isotope values for pyrite-bound sulfur ($\delta^{34}S_{pyrite}$) are most depleted in the microlaminite (down to -23‰, with the exception of the tuff at -1‰), intermediate in the lower and upper gray mudstone (down to -15‰, **Fig. 3 and 4**) but highly enriched in the black shale (up to +53‰). This isotopic enrichment coincides with the temporary drop in Fe_{PY}/Fe_{HR} with the black shale.

4.5. Elemental abundances

The transition metals broadly fall into two categories (**Table 3**): V, As, Mo, U and Cd show peaks in the black shale, whereas Cr, Co, Ni, Cu and Zn are flat or even depleted in the black shale (see **Fig. 3 and 4** for Mo and Cr as examples). In terms of enrichment factors (EF) relative to the red shales, V, As, Mo, U and Cd show clear peaks during this interval. Relative to background levels – defined here as the average EF in the gray shales – these elements are enriched in the black shale by factors of up to 4.7 for V, 5.5 for As, 110 for Mo, 8.2 for U and 9.8 for Cd (ignoring one extreme outlier in Cd enrichment). In contrast, enrichment factors of Cr, Co, Ni, Cu, and Zn are close to 1.0 throughout the section – meaning that these elements are not enriched relative to background and that they do not show any systematic trends over the studied section. The tuff bed is anomalously enriched in Cu (EF 17) and slightly enriched in Ni (EF 2.0) and Co (EF 2.3) but depleted in Cr (EF 0.4). Molybdenum and As levels are also elevated in the tuff but not exceptionally so, because these elements are already enriched in the surrounding black shales.

These contrasting enrichment patterns are also reflected in correlations with organic carbon (**Fig. 9**). Those elements enriched in the black shale show moderate to strong correlations between EF and TOC, with r^2 values of 0.70 for V, 0.43 for As, 0.61 for Mo, 0.45 for U and 0.50 for Cd. In contrast, r^2 values for Cr, Co, Ni, Cu and Zn are 0.25 or less. None of the elemental concentrations from either of the two groups correlate with pyrite sulfur abundance ($r^2 \leq 0.1$, excluding the anomalously pyritic tuff bed).

4.6. Lipid biomarker assemblage record

A broad array of biomarker ratios and abundance patterns of certain compounds can be integrated to monitor ancient biotic input and constrain paleoenvironmental facies for rocks that have experienced a sufficiently mild thermal history, as for the sedimentary rocks in this case. We used the selectivity and sensitivity of multiple reaction monitoring (MRM)-GC-MS to detect and scrutinize terpenoid alkane biomarker distributions (hopanes, steranes, methylhopanes, methysteranes and other polycyclic biomarker alkanes) alongside traditional full scan GC-MS analysis of saturated and aromatic hydrocarbon fractions prepared from rock bitumens (solvent-extractable organic matter). The hopane and sterane maturity profiles from our samples (**Table 4**) are self-consistent with the biomarker alkanes, suggesting they are syngenetic with the host strata (including similar isomer maturity patterns for hopanes and steranes regardless of carbon number; distinctive compound distributions that are not commonly associated with contaminant background signal and no detectable presence of suspicious younger biomarker features, e.g., oleanane from angiosperms). These profiles are consistent with a mid-oil-window stage of thermal maturity prior to peak oil generation. Thus, these samples were ideal targets for detailed biomarker investigation.

Key characteristics of the biomarker assemblages based on molecular ratios calculated for seven C-128 and one PT-14 samples (**Table 4**) are: (i) elevated hopane/sterane ratios (1.9-6.1) relative to the Phanerozoic marine average for organic-rich marine strata (which are generally in the 0.5-2.0 range, Rohrssen et al., 2013), (ii) moderate to high 2-methyl- and 3-methylhopane indices (Rohrssen et al., 2013), (iii) high gammacerane index values (>1.0, **Fig. 10**) that increased up section in core C-128 (the single sample from core PT-14 matches the corresponding stratigraphic interval in C-128), (iv) no detectable signal from MRM-GC-MS for 24-*n*-propylcholestanes (24-npc) from pelagophyte algae (Moldowan et al., 1990), (v) anomalously high amounts of preserved C_{40} carotanes relative to n-alkanes and (vi) low pristane/phytane ratios (<1.0). Such a combination of lipid biomarker features has been reported previously for bitumen extracts from organic matter from ancient strata attributed to saline alkaline lakes with anoxic bottom waters (Collister et al., 1990; Jiamo et al., 1990; Horsfield et al., 1994; Ruble et al., 1994; Grice et al., 1998; Summons et al., 2008). We found no detectable signals from aromatic carotenoid biomarkers – that is, markers from anoxygenic photosynthetic

bacteria such as Chlorobi – which implies that photic zone euxinia was not sustained in the water column during deposition of these strata.

5. Discussion

5.1. Testing geochemical proxies for a lacustrine depositional setting

Although the fossil record of the Newark basin preserves no evidence of marine influence (Olsen, 1988b; Olsen, 1997), many of the processes and products can inform our understanding of ancient marine settings. Of course, these rocks are also ideally suited for putting geochemical indicators of lacustrine settings to the test. One such indicator is the relationship between organic carbon and pyrite-bound sulfur (S_{py}) (Berner and Raiswell, 1984). Freshwater lakes typically display low abundances of S_{py} (< 0.2 wt.%), while TOC levels can reach many percent. In oxic marine settings, where sulfate is abundant in the water column, TOC and S_{py} typically covary in underlying sediments because a greater supply of organic carbon allows for higher rates and extents of sulfate reduction and subsequent pyrite formation (Berner and Raiswell, 1983). Sediments deposited under euxinic conditions, such as the modern Black Sea, display excess amounts of S_{py} because hydrogen sulfide accumulates in the sediments *and* the water column along with excess amounts of reactive Fe (Berner and Raiswell, 1983; Leventhal, 1983). The samples from the Towaco Fm fall outside the bounds of freshwater lakes because they are relatively enriched in S_{py} (**Fig. 7b**). This pattern is best explained by saline lacustrine conditions and the establishment of a relatively large sulfate reservoir for much of the lake history (Section 5.3). Variation in C/S ratios is most likely driven by redox changes and shrinkage of the sulfur reservoir during stratification (Section 5.2). Therefore, the C/S proxy is most straightforwardly suited to identifying freshwater lacustrine depositional settings lacking in sulfate; it is not well suited to studies of saline lakes without other indicators, such as sulfur isotope data for associated pyrite.

Along with the fossils present, however, organic biomarker data can unambiguously help to delineate non-marine settings. Specifically, the absence of 24-npc steranes (Moldowan et al., 1990) in our samples from pelagophyte algae and their ancestors, which are found exclusively in marine environments and are the dominant C_{30} sterane in marine rocks and oils of Devonian age

and younger (Gold et al., 2016), provides a strong indication of lacustrine paleoenvironments. This argument is further supported by the saline biomarker assemblage of the black shale above the fish-bearing, microlaminated portion, as well as in the upper gray shale (further discussed below). This assemblage is typical of those from saline alkaline lakes and therefore inconsistent with a marine depositional setting (Collister et al., 1990; Jiamo et al., 1990; Horsfield et al., 1994; Ruble et al., 1994; Grice et al., 1998).

5.2. Hydrological evolution

Our data and petrographic observations are consistent with previous interpretations of Van Houten cycles as products of rising and falling lake levels likely driven by climatic change in the Newark and Hartford basins (Van Houten, 1962; Hay et al., 1982; Olsen, 1986; Suchecki et al., 1988; Kruge et al., 1989; El Tabakh and Schreiber, 1994; Gierlowski-Kordesch and Rust, 1994; Olsen and Kent, 1996; Olsen et al., 1996a). The pedogenic features in the red siltstone indicate very shallow conditions with frequent exposure. The lower gray mudstone with decreasing grain size up section represents a deepening of the lake. Cross-bedding in this part of the section may reflect inputs of fluvial waters and thus a hydrologically open system at that time. The upper gray mudstone, where grain size coarsens upwards and which culminates in the upper red siltstone, likely captures a return to shallow conditions. The black shale horizon between the lower and upper gray mudstone thus represents the episode of maximum water depth (Olsen and Kent, 1996).

This conclusion is supported by the carbonate C-O isotope ratios, both of which reach a minimum in the black shale, followed by a strong up-section increase (**Fig. 3 and 4**). This pattern has been reported from Van Houten cycles in other units of the Newark and Hartford basins (Hay et al., 1982; Suchecki et al., 1988; El Tabakh and Schreiber, 1994) and is commonly observed in other closed lake basins where progressive evaporation leads to isotopic enrichments in both $\delta^{18}O_{carb}$ and $\delta^{13}C_{carb}$ (Talbot, 1990; Horton et al., 2016). Covariance between $\delta^{18}O_{carb}$ and $\delta^{13}C_{carb}$ arises because (i) evaporation favors ^{16}O- rather than ^{18}O-enriched water and (ii) increasingly saline conditions lead to a lower CO_2 solubility, and ^{13}C-enriched CO_2 is preferentially retained in the lake waters. The isotopically lightest values thus represent the deepest, most dilute end member, whereas heavy values represent relatively more evaporitic

conditions. Accordingly, the black shale horizon, including the microlaminite, where both parameters reach a minimum, should have been the freshest interval in the section bracketed by relatively evaporitic conditions before and after. It follows that the upper gray shale, where both proxies show the heaviest values, would have been the most evaporitic.

A more detailed picture can be obtained with the inclusion of the biomarker data, which indicate progressively greater contributions of halophilic organisms from the lower gray shale across the black shale and into the upper gray shale. In core C-128 core, a systematic increase in the gammacerane index (from 1.04 to 3.23) was observed up section between 52.61 m and 49.83 m, which spans the black shale interval (though excluding the microlaminite where samples were not analyzed for biomarkers). Such elevated gammacerane index values (>1) are typical of salinity stratified water columns. Carotane biomarkers, with β-carotane prominent, are also found in abundance between 50.84 m and 49.83 m of the upper black shale interval. Carotanes are diagenetic products of carotenoids, which are accessory pigments commonly found in phostosynthetic organisms; however, increased relative production of β-carotene (the precursor of β-carotane) has been reported from halotolerant modern organisms under increasing salinity (Ben-Amotz and Avron, 1983; Borowitzka et al., 1990; Fazeli et al., 2006). Additionally, the preservation of detectable carotenoids over geologic time requires relatively reducing settings due to the sensitivity of the polyunsaturated precursor molecules to rapid oxidation and degradation (Damsté et al., 1995; Hebting et al., 2006; Banta et al., 2015). The upper gray shale displays the most saline biomarker assemblage, including the highest gammacerane- and 2-methylhopane indices. This pattern suggests a progressive up-section increase in salinity across the black shale – starting above the presumably fresher fish-bearing horizon in the microlaminite – and extending into the upper gray shale. Taken together, preservation of abundant carotanes, elevated gammacerane content and the absence of the 24-npc sterane biomarkers are all consistent with a saline and redox-stratified (see also Section 5.3) lacustrine setting that persisted in the black shale above the microlaminated, fish-bearing bed.

While this pattern might seem contradictory with the C-O isotope data, which suggest that the black shale interval was fresher than the intervals above and below, it is conceivable that these proxies capture different layers in a salinity-stratified water column. Density stratification likely began during the high-stand interval, but the carbonate C-O data could reflect the relatively fresher and better mixed surface water. In contrast, the biomarkers from this interval

likely include contributions from organisms that lived in bottom waters and benthic settings that were saline and probably anoxic to favor preservation of these molecules (see also Section 5.3). It is unlikely that the biomarkers migrated down section into the black shale, as the overlying rocks are markedly less organic-rich. Hence the saline signature of the black shale is most likely indigenous to these rocks.

The ratios of sulfur isotopes and Fe_{PY}/Fe_{HR} ratios can provide additional information about the hydrological evolution of the lake basin. The sulfur isotopes are most likely controlled by biological sulfate reduction, which imparts the largest fractionations observed in the sulfur cycle, with isotopic depletions of up to 70‰ in the produced sulfide relative to the parent sulfate (Canfield, 2001; Sim et al., 2011). In a closed system, however, the sulfate reservoir can become nearly completely consumed, such that Rayleigh distillation pushes the isotopic composition of the residual sulfate and the newly formed sulfide to increasingly higher values as sulfate reduction progresses (Canfield, 2001). The positive excursion in our $\delta^{34}S_{pyrite}$ data from values as low as -23‰ in the microlaminated fish-bearing horizon to values as high as +53‰ in the black shale above the microlaminite is best explained by such a distillation process and likely reflects basin closure, stagnation and rapid consumption of the sulfate reservoir. The particularly light values in the microlaminite compared to the gray shales below (**Fig. 4**) may indicate the onset of redox-stratification where the sulfate reservoir was still relatively large, allowing for large isotopic fractionations during sulfate reduction in the anoxic portion of the water column (Lyons, 1997). Progressive depletion of the sulfate reservoir via microbial sulfate reduction, and a corresponding drop in the sulfide produced, could thus explain the observed drop in Fe_{PY}/Fe_{HR} in the black shale (**Fig. 3 and 4**). These stagnant conditions likely led to the disappearance of macrofauna.

5.3. Redox evolution

Several lines of evidence suggest that bottom waters in the Newark lake became progressively more anoxic with basin evolution marked by waning inputs and increasing evaporation: First, our molybdenum concentrations of up to 22 ppm would be rare in sediments from oxic settings because they often lack the accumulation of free sulfide in the water column that seems key to Mo enrichment (Scott and Lyons, 2012). Mechanistically, the same argument

could be applied in a lacustrine setting. Second, the high abundance of organic carbon, including the detection of unusually high relative abundances of C_{40} carotane biomarkers derived from polyunsaturated carotenoid pigment precursors prone to oxic degradation, suggests that biomass remineralization was suppressed during the deposition of the black shale due to a lack of oxygen and sulfate. The possibility of low sulfate is supported by the heavy sulfur isotopes and low pyrite abundances above the microlaminated fish-bearing horizon. Third, the decrease in bioturbation and concomitant increase in plane and wrinkly laminated black shale suggests that conditions may have become hostile for burrowing animals during deposition of the black shale, possibly in part due to low oxygen availability. Lastly, an increase in the relative abundance of anaerobic metabolisms in this ecosystem is suggested by the fairly light $\delta^{13}C_{org}$ values (Schidlowski, 1987; Zerkle et al., 2005), which may point towards a relatively higher proportion of biomass degradation by methanogens in bottom waters and in sediments.

As proposed in previous studies of other stratigraphic units in the Newark and Hartford basins, bottom-water anoxia during maximum water levels in the Van Houten cycles may have been an inevitable consequence of hydrological stagnation of the lake basin (Suchecki et al., 1988; Kruge et al., 1989; El Tabakh and Schreiber, 1994; Olsen and Kent, 1996). Saline conditions as inferred from the biomarker record starting above the microlaminite may have further suppressed the O_2 availability in these waters, as O_2 is less soluble under strongly saline conditions. Before and in particular after the deposition of the black shale, conditions were likely relatively more oxic, as indicated the much lower TOC and Mo levels. The microlaminite likely marks an intermediate stage where bottom waters were anoxic, as indicated by high Mo enrichments (**Fig. 4**), but the lake was not yet fully closed, meaning that it had an outflow and a well-oxygenated cap with abundant macrofauna (fish) and a significant sulfate reservoir, allowing for large sulfur isotope fractionations. In the gray shales with only moderately fractionated sulfur isotopes, sulfate reduction probably occurred during diagenesis in anoxic pore waters, which would explain the formation of diagenetic pyrite grains in the gray mudstone (**Fig. 5**). Hence, the water column could have been fully oxic above the gray shale-forming sediments.

The iron speciation proxy, which is commonly used to reconstruct bottom water redox conditions, is only marginally consistent with the redox trends described above. With the exception of the microlaminite, our ratios of reactive to total iron (Fe_{HR}/Fe_T) straddle the empirically defined threshold of 0.38 between oxic and anoxic settings (**Fig. 3 and 4**). This

threshold was calibrated via oxic marine sediments from continental margins around the world (Raiswell and Canfield, 1998). If we use the red siltstone from these drill cores as a detrital baseline, where three out of eleven Fe_{HR}/Fe_T ratios fall between 0.46 and 0.48 and the overall average is 0.30 ± 0.18, then the black shale (average Fe_{HR}/Fe_T = 0.40 ± 0.10, excluding the microlaminite) is only weakly enriched in Fe_{HR}/Fe_T (**Fig. 7a**). The microlaminite is the only horizon that satisfies the criterion for anoxia. Similarly, Fe_T/Al ratios stay constant throughout the drill cores outside of the microlaminite – in contrast to the Fe enrichments typically seen in anoxic settings (Lyons et al., 2003). High sedimentation rates could help the explain the lack of authigenic Fe enrichments typical of anoxic and euxinic deposition (Lyons and Severmann, 2006), because a high detrital supply drives Fe_{HR}/Fe_T and Fe_T/Al ratios toward crustal background levels. However, the relative lack of Fe_{HR}/Fe_T and Fe_T/Al enrichments in the black shales above the microlaminite may also reflect suppressed iron mobility under alkaline conditions (Section 5.5).

5.4. Evidence for elevated pH

The nitrogen isotope ratios of the Towaco Formation have probably been affected by diagenetic processes. During the degradation of biomass, in particular during the rapid degradation of peptides (Schmidt et al., 2011; Abdulla et al., 2017), nitrogen in the form of ammonium (NH_4^+) is released into pore waters. This diagenetic process is to a first order independent of redox conditions (Freudenthal et al., 2001; Schmidt et al., 2011). However, under oxic conditions, nitrification of diagenetic NH_4^+ results in a net increase in the residual $\delta^{15}N$ of biomass by a few permil (Freudenthal et al., 2001; Lehman et al., 2002). This process may largely explain the values around +5‰ in the gray shales of the Towaco Formation. However, the spike to +15‰ in the black shale above the microlaminated fish-bearing interval is too large to be the result of diagenetic alteration alone. In fact, under anoxic conditions, as inferred from this part of the section, the diagenetic isotope effect is negligible (Freudenthal et al., 2001; Lehman et al., 2002; Robinson et al., 2012).

Such high values require processing of fixed nitrogen in the water column. In modern freshwater lakes, $\delta^{15}N$ typically falls between 0‰ and +6‰ (McLauchlan et al., 2013), and marine sediments only display higher values of up to +15‰ in upwelling zones with high

degrees of denitrification, made possible by a large supply of dissolved nitrate from the deep ocean, which allows for such a signal to be preserved despite extreme nitrate loss (Tesdal et al., 2013). In lakes, however, strongly elevated $\delta^{15}N$ have only been reported from alkaline settings (Collister and Hayes, 1973; Talbot and Johannessen, 1992; Lent et al., 1995; Menzel et al., 2013; Stüeken et al., 2015c). Under high-pH conditions, diagenetically released NH_4^+ can partition into volatile NH_3 with a pKa of 9.25. This partition reaction is associated with a large isotopic fractionation of 45‰ at standard temperature, where residual NH_4^+ becomes isotopically heavier as NH_3 escapes into the atmosphere (Li et al., 2012). Preservation of the non-volatile NH_4^+, which can be re-assimilated into biomass and incorporated into clay minerals by substituting for K^+ (Müller, 1977; Schroeder and McLain, 1998), renders residual sediments isotopically heavy. The nitrogen isotope data from the Towaco Formation with $\delta^{15}N$ values up to 15‰ may thus point to strongly alkaline conditions with a pH around 9 or higher during the deposition of the black shale, such that NH_3 production was favored and $\delta^{15}N$ increased. Such high pH may have contributed to the disappearance of macrofauna and hence the absence of fish fossils above the microlaminite.

It is conceivable that the water column was relatively alkaline throughout the rest of the lake history, consistent with the biomarker assemblages throughout the section. However, the effect of NH_3 volatilization may only have been expressed under stratified conditions where NH_4^+ and NH_3 were able to escape nitrification and build up in the water column. This scenario is exemplified by modern Mono Lake in the western U.S. (pH ~ 10), where stratification has led to accumulation of a large NH_4^+/NH_3 reservoir in bottom waters that is only released into the atmosphere during seasonal water-column overturn (Jellison et al., 1993).

This interpretation is consistent with the high ratios of total carbon over total nitrogen (hereafter C/N) in our black shale. The transformation of NH_4^+ to NH_3 during diagenesis would have led to a strong preferential loss of nitrogen from sediments relative to carbon, because uncharged NH_3 is less amenable to incorporation into clay minerals. This process can therefore explain the observed positive excursion in C/N ratios in the black shale. It is unlikely that the high C/N ratios reflect terrestrial plant biomass (which is known to have high primary C/N ratios > 30, McGroddy et al., 2004; Reich and Oleksyn, 2004), because the high C/N ratios in the Towaco Formation coincide with light $\delta^{13}C$ values (**Fig. 3 and 4**), which are uncharacteristic of Jurassic flora (Whiteside et al., 2011). Most of the biomass in the black shale is thus likely to be

microbial (see also Spiker et al., 1988), which typically has primary C/N ratios around 7-10 (Godfrey and Glass, 2011). The measured excursion in C/N up to 50 therefore most likely reflects enhanced N loss from the system during alkaline NH_3 volatlilization.

The observed correlation between C/N ratios and TOC in the Towaco Formation (**Fig. 6b**) may be the result of greater NH_4^+ and NH_3 production under relatively more anoxic conditions. When less O_2 gets mixed into the sediments, more organic carbon can be preserved, and less NH_4^+/NH_3 gets oxidized to NO_3^-. Hence, more nitrogen could be lost as NH_3 and drive $\delta^{15}N$ of residual NH_4^+ heavy, which would then get passed on to biomass and clay minerals.

We speculate that the kinks in the slope in **Fig. 6a and 6b**, where $\delta^{15}N$ increases more strongly above C/N > 35 (**Fig. 6a**), and C/N ratios increase less strongly where TOC is above ~2% (**Fig. 6b**), reflect the establishment of thermal and/or salinity-driven stratification of the water column – similar to Mono Lake (Jellison et al., 1993). During this stratified phase, the isotopically heavy NH_4^+ may have become a more important source of fixed nitrogen for microbes in the photic zone, such that sinking biomass was already enriched in $\delta^{15}N$ prior to diagenesis, leading to higher overall $\delta^{15}N$ values in sediments.

5.5. Effects of high pH on metal cycling

If the Newark basin did indeed become alkaline with the onset of evaporation after the deposition of the microlaminite as a deep-water facies, leading to pH values approaching values of 9 or higher (favoring NH_3 loss), then this may explain some of the patterns in our iron and trace element data. As noted above (Section 5.3) and by previous studies on other parts of the Newark and Hartford basins (Van Houten, 1962; Kruge et al., 1989; El Tabakh and Schreiber, 1994; Olsen and Kent, 1996), the black shale in the Van Houten cycle most likely marks an episode of bottom-water anoxia, and we see evidence thereof in the iron speciation data of the microlaminite. Yet Fe_T/Al ratios in the overlying black shale are only weakly enriched compared to the red siltstone, and Fe_{HR}/Fe_T ratios even show a drop in the middle of the black shale in core C-128 above the microlaminite (**Fig. 4**). High sedimentation rates may have contributed to the lack of enrichment in authigenic Fe phases; however, high pH would have suppressed iron mobility and thus the potential for enrichment under anoxic conditions.

The Fe_T/Al and Fe_{HR}/Fe_T redox proxies rely on the fact that iron is typically soluble as Fe^{2+} in anoxic waters and can thus accumulate as authigenic iron minerals in sediments that are deposited beneath an anoxic water column. Compared to sediments from oxic settings, anoxic sediments with low sedimentation rates typically show high Fe_T/Al and Fe_{HR}/Fe_T ratios relative to oxic baselines (Raiswell and Canfield, 1998; Poulton and Raiswell, 2002; Lyons et al., 2003; Lyons and Severmann, 2006; Raiswell, 2011; Clarkson et al., 2014). Empirically, the oxic-anoxic threshold lies at around 0.38 for Fe_{HR}/Fe_T and 0.55 ± 0.11 for Fe_T/Al for oxic marine sediments and ancient equivalents (Raiswell and Canfield, 1998; Clarkson et al., 2014). However, these proxies can only work if dissolved iron can enter the water column of a sedimentary basin. In marine basins, dissolved iron can be introduced either by hydrothermal inputs or from diagenetic pore fluids on the continental shelf where ferric iron oxides are reduced to Fe^{2+} and expelled into the water column and transported (Lyons, 1997; Wijsman et al., 2001; Anderson and Raiswell, 2004; Severmann et al., 2008; Raiswell, 2011). The latter source is known as the intra-basinal iron shuttle.

In the lacustrine Newark basin we have no clear evidence for hydrothermal input, thus the iron shuttle would probably have been the only source of dissolved iron to the water column. This source can be sufficient to generate high enrichments in authigenic iron under anoxic conditions as exemplified by the modern Black Sea (Lyons, 1997; Wijsman et al., 2001). Importantly, however, the solubility of Fe^{2+}drops by more than an order of magnitude with a one-unit increase in pH (Morgan and Lahav, 2007; Lewis, 2010). If the pH of the Newark basin reached values around 9 or higher, it is conceivable that Fe^{2+} produced from diagenetic reduction of iron oxide particles was mostly trapped in pore waters rather than being expelled into the water column, making the iron shuttle significantly less efficient than in marine environments or even less alkaline lakes. Indeed, the black shale and the gray mudstones in the Towaco Formation show a high abundance of carbonate-bound iron (Fe_{carb}) in association with relatively lower Fe_{PY}/Fe_{HR} (**Fig. 8**). Fe^{2+} may thus have been trapped immediately in diagenetic Fe-carbonate rather than entering the dissolved load – in particular in the upper gray shale, which was presumably the most saline and alkaline based on C-O isotope data and biomarkers (Section 5.2). The subtle enrichments in Fe_{HR}/Fe_T in the black shale and lower gray mudstone suggest that the iron shuttle was probably not completely muted and possibly sustained through organic

complexation of iron. But the general lack of response in Fe_T/Al and the small drop in Fe_{HR}/Fe_T in the black shale in core C-128 suggest that iron was overall not highly mobile in this setting.

Like iron, other transition metals may have been affected by high pH (Lewis, 2010). Tack *et al.* (1996) reported a decrease in the solubility of Cu, Pb, Zn, Co, Ni, Mn and Cd with increasing pH in experiments with marine sediments, which they attributed to a combination of two factors: incorporation of divalent cations into carbonate and/or adsorption onto iron oxides. Before we evaluate these two possible sinks for the Newark Basin, we stress that the *absolute* magnitude of metal enrichments in our samples is not comparable to a marine setting because the overall reservoir of metals is likely smaller in a lake than it is in the ocean. However, lakes also have a smaller metal sink, which may scale to some degree with the smaller reservoir size. Furthermore, and most importantly, the *relative* differences in the behavior of different metals may plausibly be explained by their distinct response to pH conditions. We will therefore focus on comparing the general behavior of different groups of metals rather than interpreting their absolute enrichment factors.

Regarding carbonate, Harrison *et al.* (1973) observed a predominance of carbonate-bound Cd, Co, Mn and Zn in rocks of the Green River Formation, which accumulated in an Eocene alkaline lake. Carbonate-trapping on the basin margin, possibly during diagenesis, may thus explain why we did not find enrichments in Co, Ni, Cu and Zn in the Towaco black shale. Similar to Fe^{2+}, these elements may not have been released into the dissolved phase. However, we do observe a moderate enrichment in Cd, which also has a high affinity for carbonate (Zachara et al., 1991) and thus should not have been mobilized from porewaters under these alkaline conditions. This discrepancy may point to adsorption onto iron oxides as a more important mechanism by which cationic transition metals were trapped on the basin margin. In general, the adsorption affinity of cations on iron and manganese oxides increases with increasing pH, because iron oxide surfaces become more negatively charged and thus more attractive for cations (Stumm and Morgan, 1996). Cadmium, however, has the lowest adsorption affinity compared to Co, Ni, Cu and Zn (Abd-ElFattah and Wada, 1981; Tiller et al., 1984; Bruemmer et al., 1988). We therefore speculate that under alkaline conditions in the Newark lake most of the cationic metals – with the exception of Cd – were trapped efficiently by shallow-water red beds, thus lowering their overall dissolved inventory and enrichment in the deeper

basin. Trapping by carbonates may have occurred during diagenesis but was perhaps quantitatively less important than iron oxide adsorption in lowering dissolved metal levels.

Vanadium, As and Mo, which generally form oxyanions in water, show solution behaviors opposite those of cationic metals. Their affinity for adsorption onto iron oxides drops with increasing pH because the surfaces become more repulsive (Stumm and Morgan, 1996; Zinabu and Pearce, 2003), and Mo has been shown to be more soluble at high pH even in the presence of high H_2S levels (Helz et al., 2011). Also, U solubility increases with pH as dissolved U(VI) is stabilized by carbonate complexation (Casas et al., 1998; Maher et al., 2013). In the alkaline Newark basin, these elements could thus have built up in solution. Their only sink would have been biological uptake, adsorption onto biomass and minor pyrite uptake in anoxic bottom waters (where pyrite is rare), which would explain their strong correlations with TOC (**Fig. 9**). Chromium also forms a soluble oxyanion in its most oxidized form, Cr(VI), and should thus behave like V, As and Mo – counter to what we observed in the drill cores. However, Cr in rocks is primarily present as Cr(III), which forms insoluble $Cr(OH)_3$ at high pH, thereby slowing down the oxidation rate and suppressing the mobility of Cr in solution (Eary and Rai, 1987; Zayed and Terry, 2003). Chromium may thus not have been mobile in the Newark lake waters, which would explain why it shows no enrichment in the black shales of the Towaco Formation.

6. Synthesis of basin evolution

The studied section of the Towaco Formation in the early Jurassic Newark basin records the deepening and shallowing of an ancient rift lake, likely driven by cyclic climatic changes (Van Houten, 1962; Olsen, 1986). As suggested by our biomarker records, the lake waters likely became progressively more saline and alkaline with increased evaporation above the microlaminated fish-bearing unit. In fact, increased salinity stratification, which would have promoted redox stratification between upper and lower water layers, was likely a major factor in enhancing organic matter preservation during deposition of the black shale interval as evidenced by the high gammacerane index values and abundant carotane preservation in chromatograms. Bottom-water anoxia prevailed only during the deposition of the black shale, as indicated by the accumulation of Mo, which probably marks an episode of stagnation and stratification as suggested for Van Houten cycles elsewhere in the basin (Kruge et al., 1989; El Tabakh and

Schreiber, 1994) and may explain the disappearance of macrofauna at this time. These observations may be synthesized as follows (from oldest to youngest):

Phase 1 – wet stage in a warm climate: During deposition of the lower gray shale, water influx exceeded loss by evaporation, such that the lake became progressively deeper. The shallow depth of the lake during this time likely allowed for wind mixing and entrainment of atmospheric oxygen into the water column, which would explain the observed ripples and the lack of authigenic iron and trace metal enrichments.

Phase 2 – climatic turning point towards arid conditions: When the lake reached its maximum depth, likely marked by the microlaminite, the lake was evidently sufficiently dilute to support a rich biota that included various fish species (Olsen, 1988b; Olsen et al., 2003). However, oxygen contents began to decrease in the bottom waters at this time as indicated by our iron and Mo data. During subsequent deposition of the remainder of the black shale, evaporation became more important for the chemical properties of the sediments, leading to high salinity, high alkalinity and stagnation, as indicated by the biomarkers and the preservation of undisturbed wrinkly mats on the lake floor. Saline waters sank to the bottom, beneath a fresher surface cap. The carbonate C-O isotope data likely capture this freshwater cap. Stagnation, paired with low O_2 solubility in saline waters, enhanced anoxia in deep waters. NH_3, built up in the lower anoxic alkaline water column, was perhaps released to the atmosphere during seasonal overturn – as we see in modern alkaline lakes. This process would explain the large $\delta^{15}N$ values observed in the black shale.

Phase 3 – arid climate: During deposition of the upper gray shale, salinity increased further, as suggested by the biomarkers and oxygen isotope data. Evaporation exceeded inflow and the lake level dropped. Under shallow conditions, wind mixing extended down to the sediments, allowing for the formation of ripples and the entrainment of oxygen. Finally, deposition of the red shales marks complete desiccation with only seasonal or less frequent flooding.

7. Conclusions and broader implications

The Newark basin, whose hydrological evolution can be constrained by sedimentary features, isotopic indicators, biomarkers and paleogeographic reconstructions, can serve as a

natural laboratory for assessing the effects of high pH on environmental proxies. Our data suggest that under such conditions some of the commonly used redox proxies behave differently compared to behaviors under circumneutral pH. Ratios of Fe/Al and Fe_{HR}/Fe_T, which are commonly enriched in marine anoxic settings, show no significant difference between the oxic and anoxic alkaline facies in the Towaco Formation. Only the microlaminite unit, which probably marks the beginning of anoxic bottom waters immediately before lake shrinkage by evaporation, shows the authigenic iron enrichments that one would expect under anoxic conditions. These enrichments are not expressed in the subsequent alkaline facies, although anoxia likely persisted. Of the minor elements, Mo, As, V, U and Cd are enriched in the alkaline black shale facies, but Co, Ni, Cu, Zn and Cr are not. These patterns are most parsimoniously explained by differential pH effects on the solubility of the elements: iron, Co, Ni, Cu, Zn and Cr become less soluble with increasing pH, whereas Mo, As, V, and U are more soluble.

To first order, the solubility of transition metals in the ocean is controlled by the redox state and H_2S inventory of the water column. However, pH may in part dictate the magnitude of enrichment in marine sediments. For example, Mo concentrations in euxinic marine black shales increase strongly from the Proterozoic to the Phanerozoic in response to oxygenation of the deep ocean (Scott et al., 2008), but Zn shows only a relatively weak change across this interval (Scott et al., 2012). A number of explanations are plausible, including a high flux of hydrothermal Zn into the Precambrian oceans or stabilization of Zn by organic complexes. However, in light of recent modeling that suggests an increase in seawater pH from around 6.5 in the Archean to modern values close to 8.0 (Halevy and Bachan, 2017), it is also possible that the difference in behavior between Mo and Zn was at least in part modulated by pH. Molybdenum would have become relatively more soluble over time, whereas the solubility of Zn would have decreased. This effect would not impact inferences about ocean oxygenation, but it may play a role for the relative sensitivities of the different proxies.

Another important aspect for ocean redox evolution may be the decreasing solubility of ferrous iron with increasing pH (Morgan and Lahav, 2007; Gudbrandsson et al., 2011). Ferrous iron was the major redox buffer in the Archean and Proterozoic deep ocean (Poulton and Canfield, 2011). If seawater pH increased through Earth's history, then the resulting drop in iron solubility should have lowered the concentration of dissolved Fe^{2+} in the water column, which may ultimately have helped facilitate global oxygenation. Despite the many remaining

unanswered questions and the multiple possible interpretations, our results stress that redox proxies do not necessarily respond to redox changes in a linear fashion, and other parameters, including pH, deserve more attention in future studies. Within this context, diverse proxies, alone and in combination, may help us delineate and characterize ancient alkaline systems.

Acknowledgements

This work was supported at the University of California, Riverside by the NSF-EAR FESD Program and the NASA Astrobiology Institute under Cooperative Agreement No. NNA15BB03A issued through the Science Mission Directorate. We thank Roger Buick (UW) for financial support of the carbon and nitrogen isotope work. EES acknowledges support from a NASA postdoctoral fellowship, as well as valuable discussions about the Newark basin with Charlotte B. Schreiber. GDL thanks the Agouron Institute for providing funding for the Waters Autospec GC-MS instrument at UCR. We thank Dr. Wang (China University of Petroleum) for help with sampling, the Rutgers core repository for access, and Andy Robinson, Bridget Lee (UCR) and Andy Schauer (UW) for technical support. The manuscript benefitted from constructive comments by Brian Stewart, Jessica Whiteside, and one anonymous reviewer.

Figure captions

Figure 1: Geologic map of the Newark Basin. The early Jurassic Towaco Formation investigated in this study is highlighted in blue. The Triassic-Jurassic boundary lies within the Passaic Formation. Adapted from Olsen *et al.* (1996a).

Figure 2: Facies evolution and distribution. A: The lake basin formed in a half-graben where activity along the normal fault created accommodation space for sedimentation (adapted from Olsen, 1988b). Our sample set captures the marginal/shoreline facies (red siltstone), the shallow lake facies (gray mudstone) and deep lake facies (black shale). B: Schematic of a Van Houten cycle of lake deepening and shallowing in the Towaco Formation as inferred from the sedimentary record (adapted from Olsen, 1997). LRS = lower red siltstone, LGM = lower gray mudstone, BS = black shale, UGM = upper gray mudstone, URS = upper red siltstone. The purple interval depicted here was not prominent in our study section.

Figure 3: Chemostratigraphy of core PT-14 through the Towaco Formation. Panel A: Elemental abundances. Enrichment factors (EF) for Mo and Cr were calculated relative to the average of all red shales in the two cores. B: Isotopic ratios and additional abundance data. The fish-bearing horizon, which could not be analyzed, is immediately at the base of the black shale where sulfur isotope values are most negative. The dashed lines in the iron speciation graph show the empirically defined thresholds for the transitions from oxic to anoxic conditions (Fe_{HR}/Fe_T > 0.38, Raiswell and Canfield, 1998) and from ferruginous to euxinic conditions (Fe_{PY}/Fe_{HR} > 0.7 and FeHR/FeT > 0.38, Poulton and Canfield, 2011). The solid red line marks the average Fe_{HR}/Fe_T ratio of all red stilstones from both drillcores. In the Fe_T/Al panel, the solid red line also marks the red siltstone average. This comparison highlights that the black shale is not significantly enriched in authigenic iron compared to background sediments. Light shaded green bar = water level increase as inferred from lithofacies (grain size fining). Dark shaded green bar = water level highstand and thermohaline stratification as inferred from lithofacies and $\delta^{18}O_{carb}$. Shaded blue bar = water level shrinkage by evaporation as inferred from $\delta^{18}O_{carb}$ and biomarkers.

Figure 4: Chemostratigraphy of core C-128 through the Towaco Formation. Symbols and shading as in Fig. 3.

Figure 5: Images of rocks in the Towaco Formation. A, B, C, E and F are photomicrographs that were taken with a microscope camera, D is a photograph of a thin section. **A:** PT-14, 102.29m, bioturbated intermingled siltstone and mudstone with subordinate diagenetic carbonate; **B:** PT-14, 98.04m, massive mudstone with euhedral diagenetic pyrite (opaque grains); **C:** C-128, 47.06m, interbedded silt sheets and micro-turbidites with graded lamination from silt to mud; **D:** C-128, 51.54m; plane-to-wrinkly laminated carbonaceous, calcareous shale, highlighting absence of bioturbation in hand-sample view; **E:** C-128, 51.11m, plane-to-wrinkly

laminated carbonaceous, calcareous shale where light-colored laminae are carbonate-rich; **F:** PT-14, 99.85m, close-up of carbonaceous wrinkly laminae in the black shale, bracketed by carbonate-rich laminae with micritic matrices and small sparry fenestrae.

Figure 6: Carbon-nitrogen scatter plots. A: bulk $\delta^{15}N$ versus organic carbon to total nitrogen (C/N) ratios. The kink in the slope likely indicates the onset of stratification and build-up of an isotopically enriched NH_4^+ reservoir in the water column that became bioavailable to algae and prokaryotes. B: C/N ratios versus total organic carbon (TOC). The correlation between the two parameters likely suggests higher rates of NH_4^+/NH_3 production and NH_3 loss from biomass (increasing C/N) under progressively more anoxic conditions that favor increasing TOC buildup. The kink in the slope may reflect a transition towards stratification and seasonal NH_3 release as in modern Mono Lake (Jellison et al., 1993). C: Bulk $\delta^{15}N$ versus organic $\delta^{13}C$ isotopes. The interval of heaviest $\delta^{15}N$ – interpreted as redox stratified – is characterized by light $\delta^{13}C$, which may indicate anaerobic metabolisms or utilization of isotopically light DIC in a stratified water column. D: TOC versus organic $\delta^{13}C$, showing that that anaerobic metabolisms (light $\delta^{13}C_{org}$) correspond to intervals of high biomass accumulation, consistent with redox stratified conditions.

Figure 7: (a) Iron speciation. Highly reactive over total iron (Fe_{HR}/Fe_T) versus pyrite-bound over highly reactive iron (Fe_{PY}/Fe_{HR}). The black and gray shale are only weakly enriched in Fe_{HR}/Fe_T relative to the red siltstone. Note that three out of eleven data points from the red siltstone have Fe_{HR}/Fe_T ratios between 0.46 and 0.48, which is nearly the same as in the most enriched black and gray shales. The intrabasinal iron pump may thus have been acting less efficiently than in marine settings, though it was probably not completely muted. Black dashed lines = empirically defined thresholds from global sample collections (Raiswell and Canfield, 1998; Poulton and Canfield, 2011); red solid line and shaded area = average Fe_{HR}/Fe_T ratio ± 2 SD from the red siltstones in the two studied drill cores of the Towaco Formation. **(b) Pyrite-bound sulfur (S_{py}) versus total organic carbon (TOC).** The highest C/S ratios occur in the middle of the black shale, concurrent with maximum TOC and $\delta^{15}N$ values; the lowest C/S ratios coincide with the highest S_{py} abundances in the lower gray shale (Fig. 3 and 4). Trends for freshwater lakes and marine sediments are taken from the literature (Berner and Raiswell, 1983; Berner and Raiswell, 1984; Lyons et al., 2000). The "marine Holocene" trendline shows the average covariance between S_{py} and TOC in marine sediments from oxic settings. The "marine post-Silurian" trend accounts diagenetic and metamorphic loss of organic carbon, which leads to a steeper trendline in sedimentary rocks from oxic marine settings. The 'post-Silurian' selection accounts for the presence of some vascular plant biomass, which is more recalcitrant and less prone to carbon loss during diagenesis and metamorphism (Raiswell and Berner, 1987). Even older sedimentary rocks, or samples from settings with no input of plant biomass, would display an even steeper trendline.

Figure 8: Iron speciation in stratigraphic context. Iron phases that make up highly reactive iron (Fe_{HR}) change systematically across the section. In the red siltstone, ferric iron oxides (Fe_{HEM}) dominate; in the lower gray mudstone and the black shale, pyrite-bound iron (Fe_{PY}) dominates and in the upper gray mudstone, carbonate-bound iron (Fe_{CARB}) is most abundant.

Fe_{CARB} also shows a spike in the middle of the black shale where Fe_{PY} drops, and it is relatively abundant at the base of the lower gray mudstone. The distribution of Fe_{CARB} does not follow carbonate abundances (Fig. X and Y), indicating that it is not a simple equilibrium process proportional to Fe^{2+} abundance in the lake water column. This is consistent with Fe^{2+} retention in pore waters by diagenetic carbonate.

Figure 9: Trace metal enrichment factors (EF) versus total organic carbon (TOC). In all panels, gray dots = core C-128; black diamonds = core PT-14. Upper row = elements that show enrichments in the black shale; lower row = elements that show no systematic variability across the two cores and no enrichments in the black shale. Enrichment factors are calculated relative to the average of all red shales in the two cores. In panel D, one outlier with Cd (EF) = 44.3 at TOC = 2.83% from core PT-14 was excluded.

Figure 10: Biomarker patterns. MRM-GC-MS traces comparing C_{30} triterpane distributions (using the appropriate molecular-daughter ion transition of 412-191 Da for selective detection of these polycyclic alkanes) for different rock bitumen extracts from the C-128 core. Compound peaks identified are: 1. C_{30} diahopane; 2. C_{30} αβ-hopane; 3. C_{30} βα-hopane (moretane); 4. gammacerane. A systematic reduction in the abundance of gammacerane (4) relative to C_{30} αβ-hopane (2) with increasing depth in the black shale interval suggests the upper portion of black shale was deposited in a more saline and likely progressively shallowing lacustrine setting. Even higher relative abundances of gammacerane are found in the two organic-lean silty shales in the overlaying evaporative section (see Table 4), presumably reflecting periodic hypersaline depositional conditions for this shallow upper stratigraphic interval.

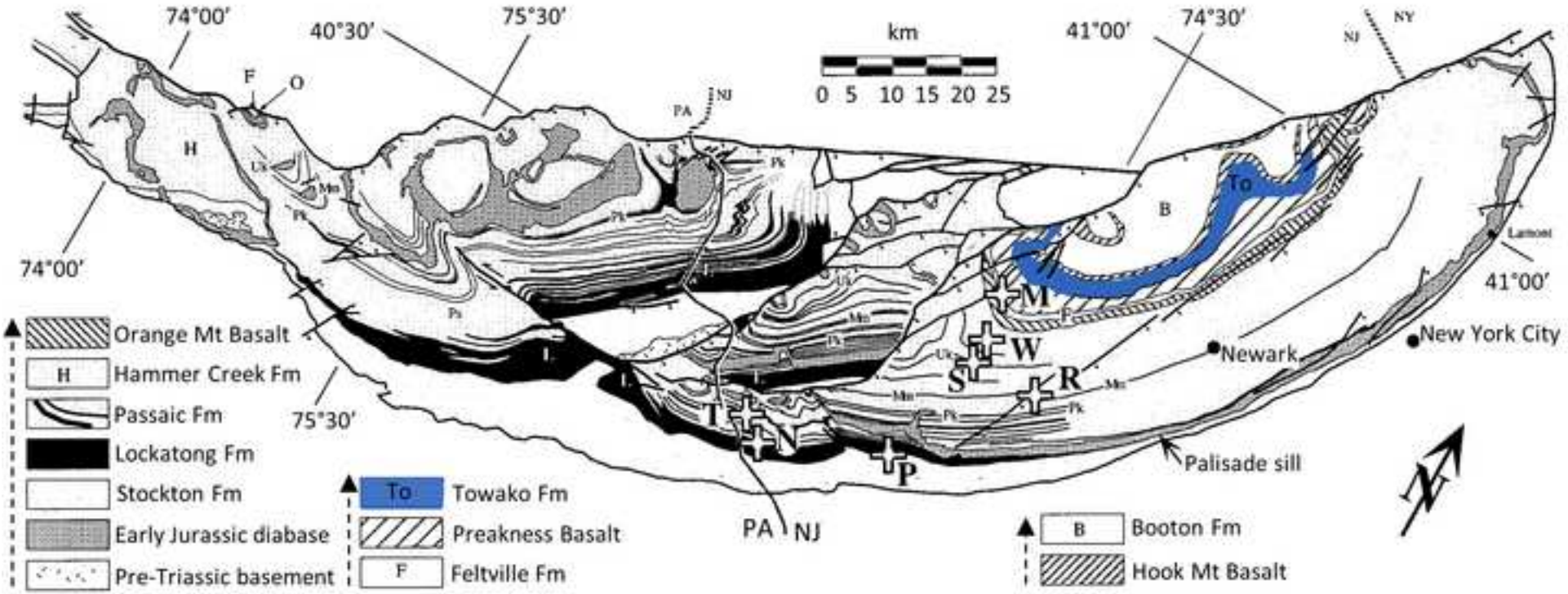

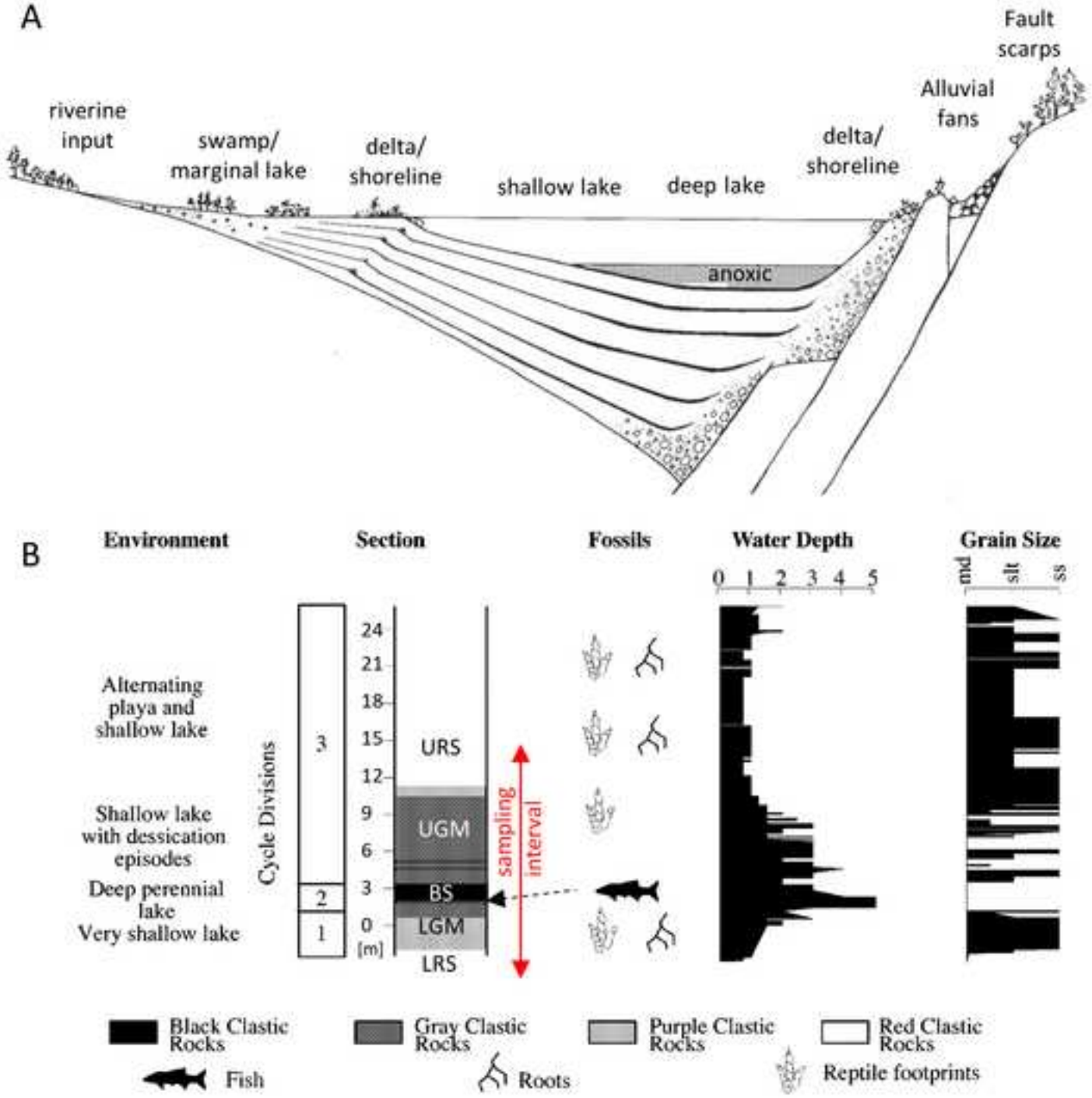

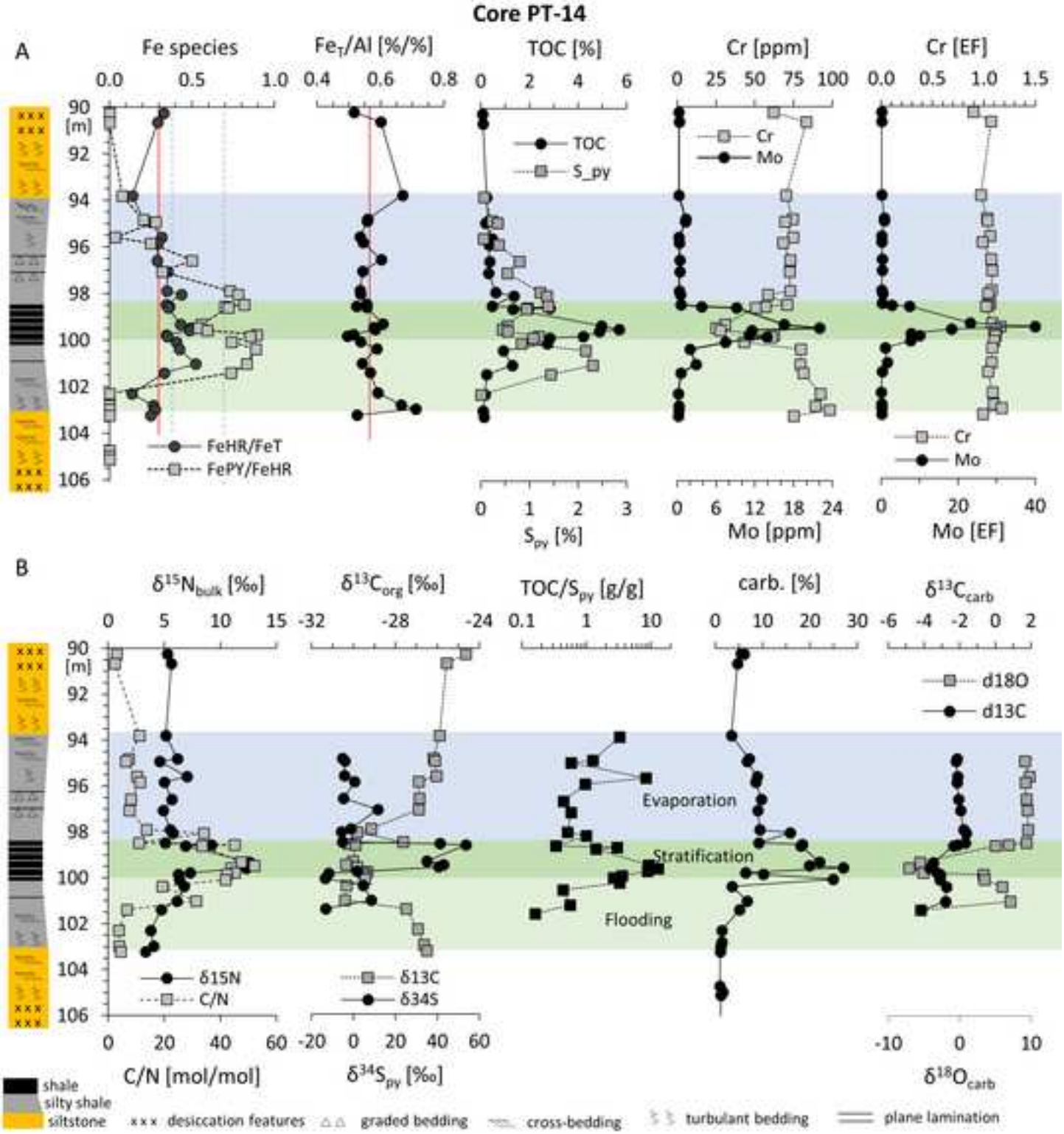

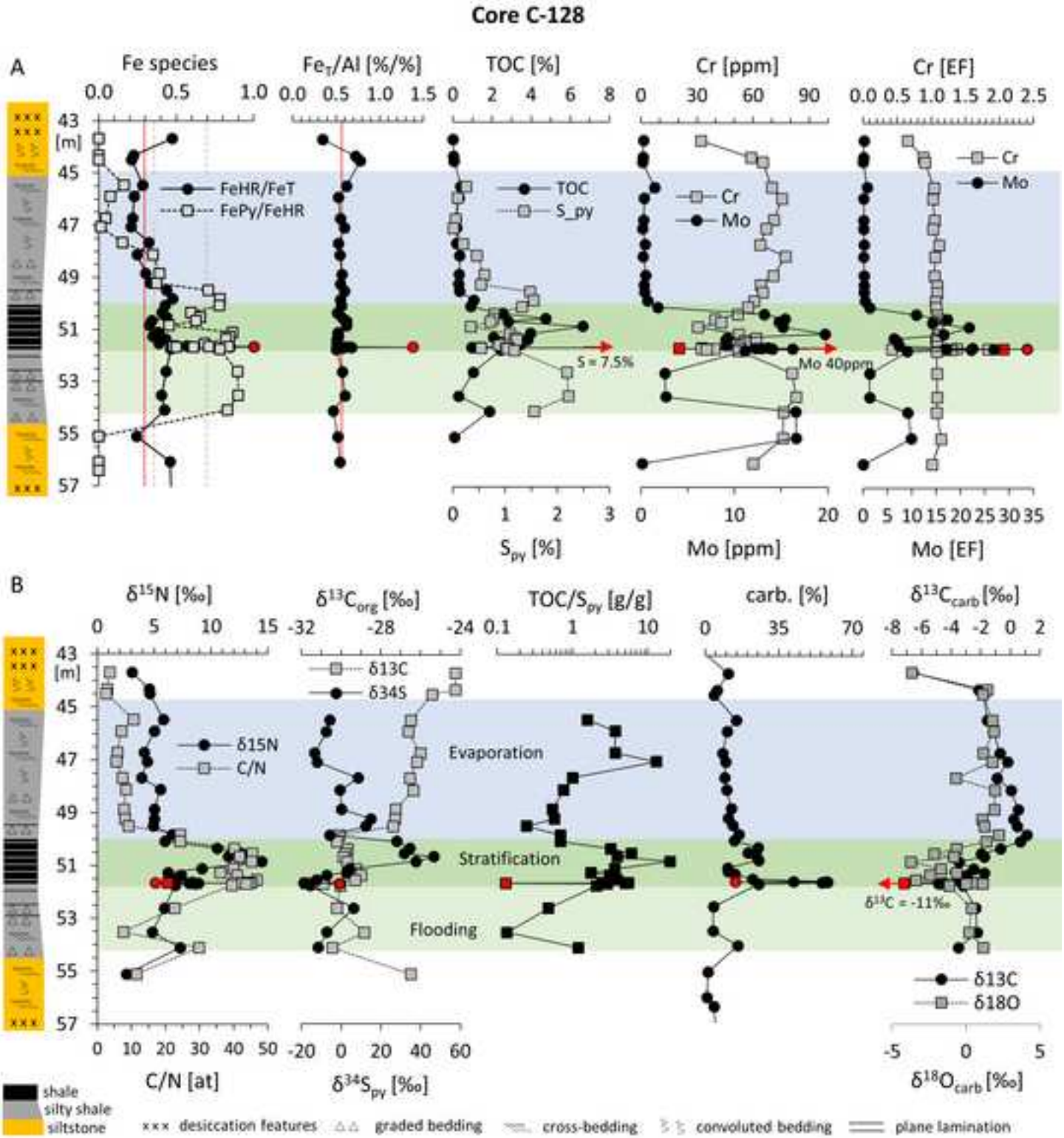

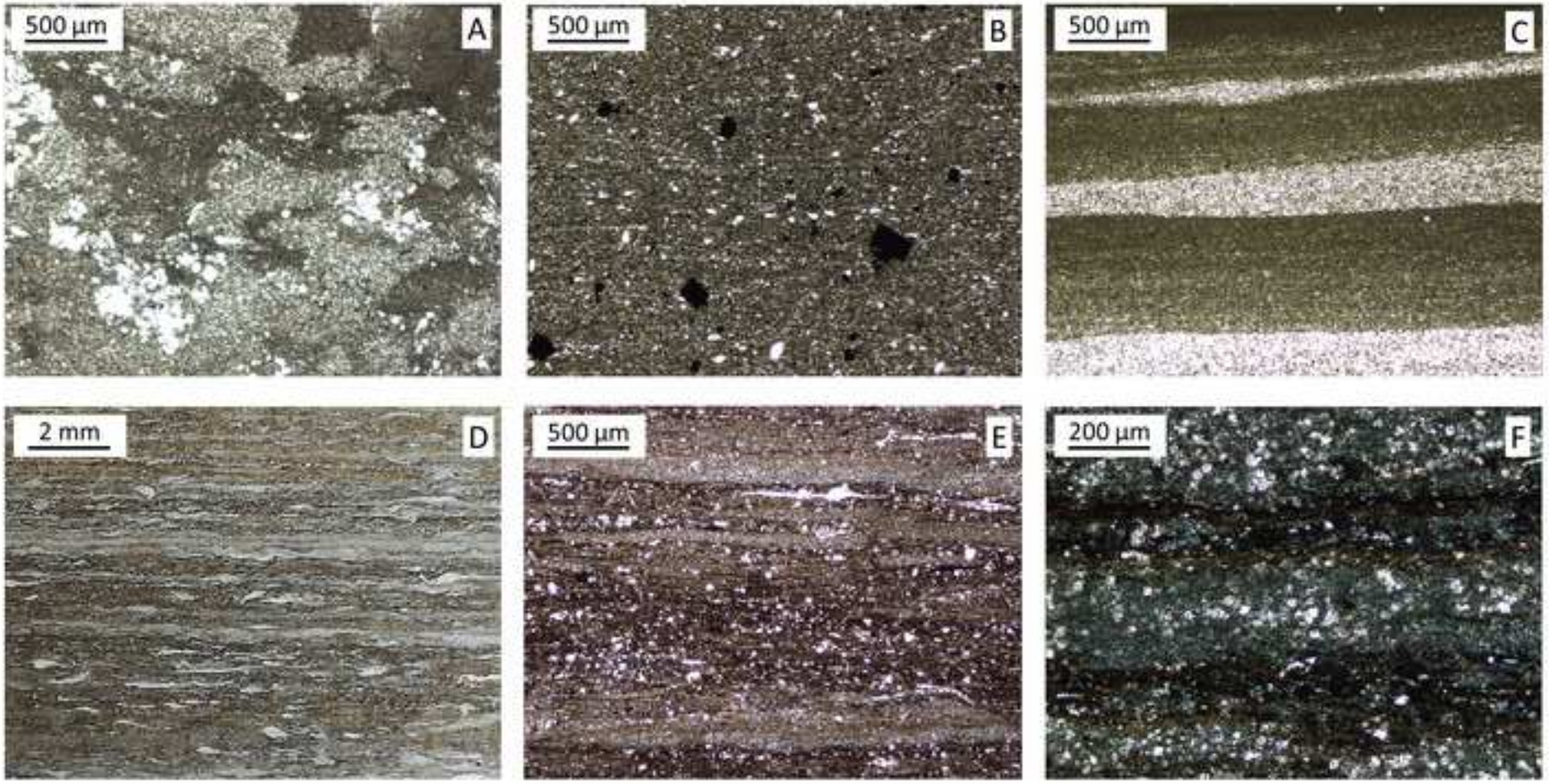

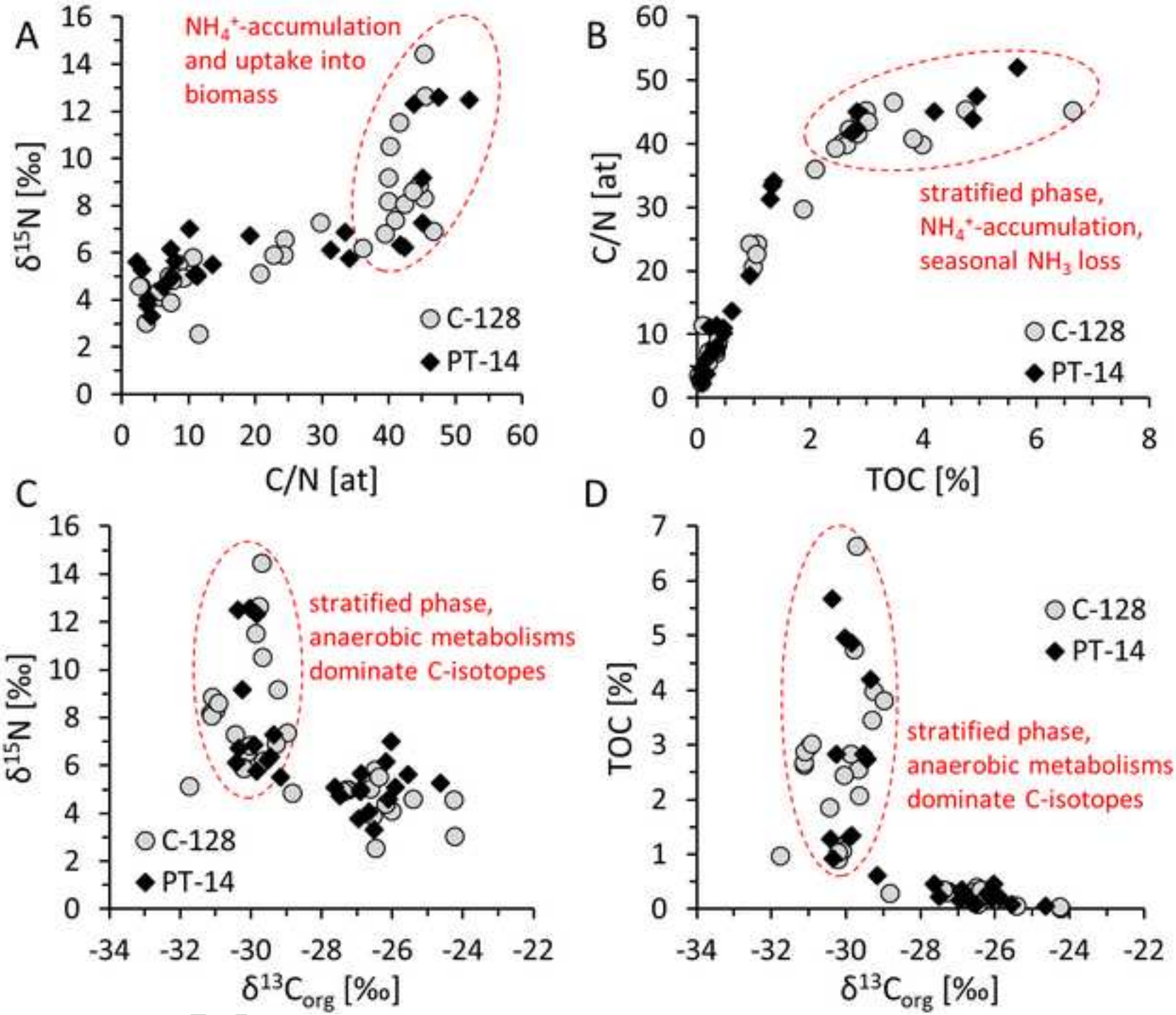

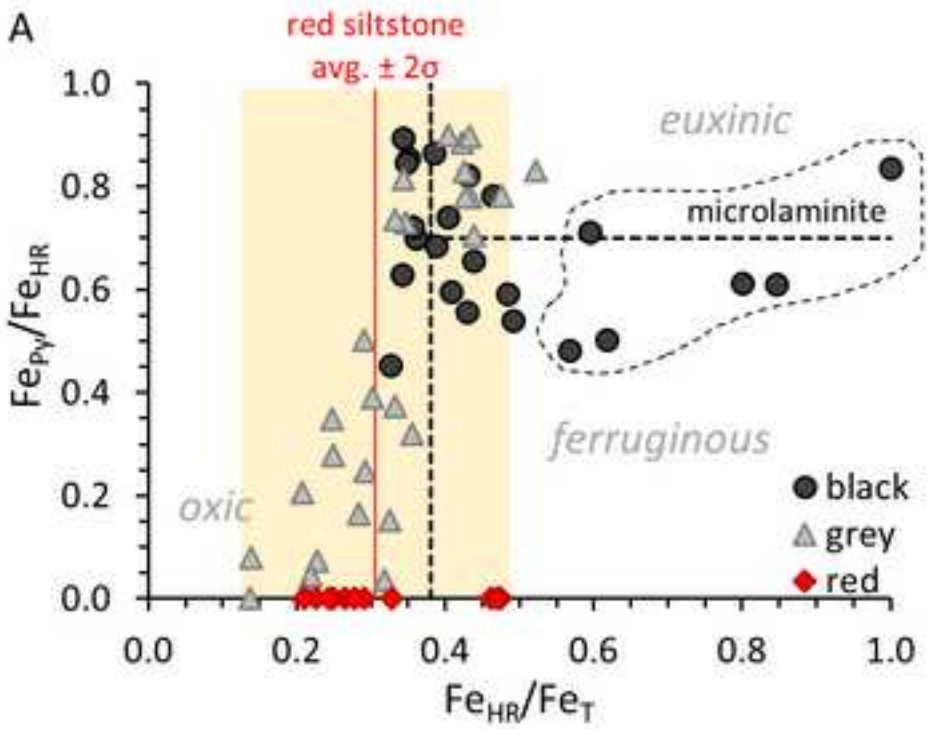

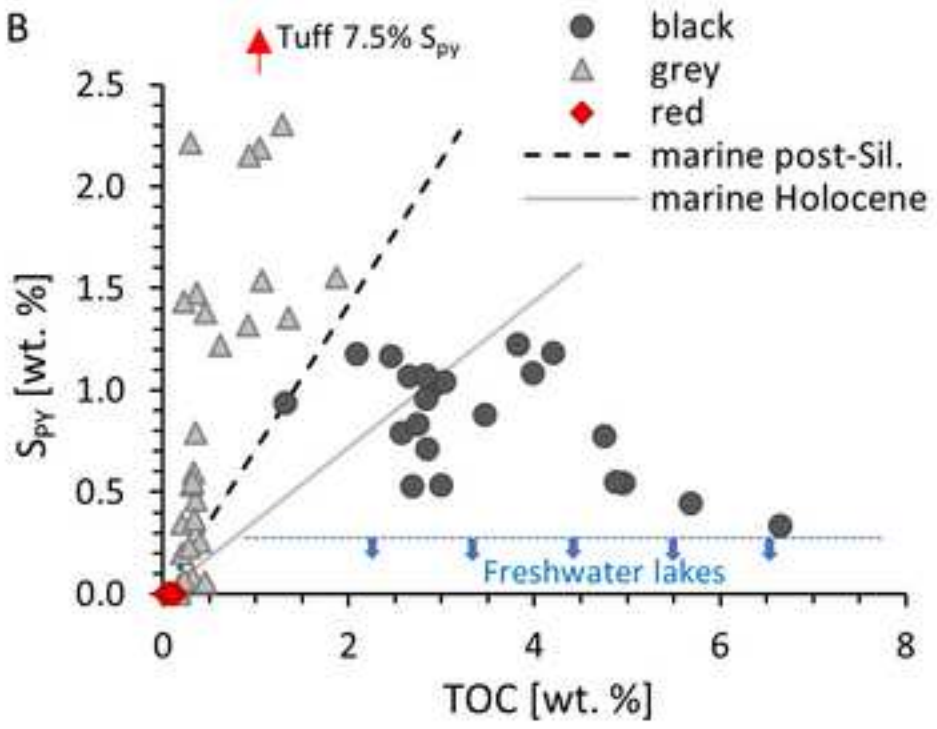

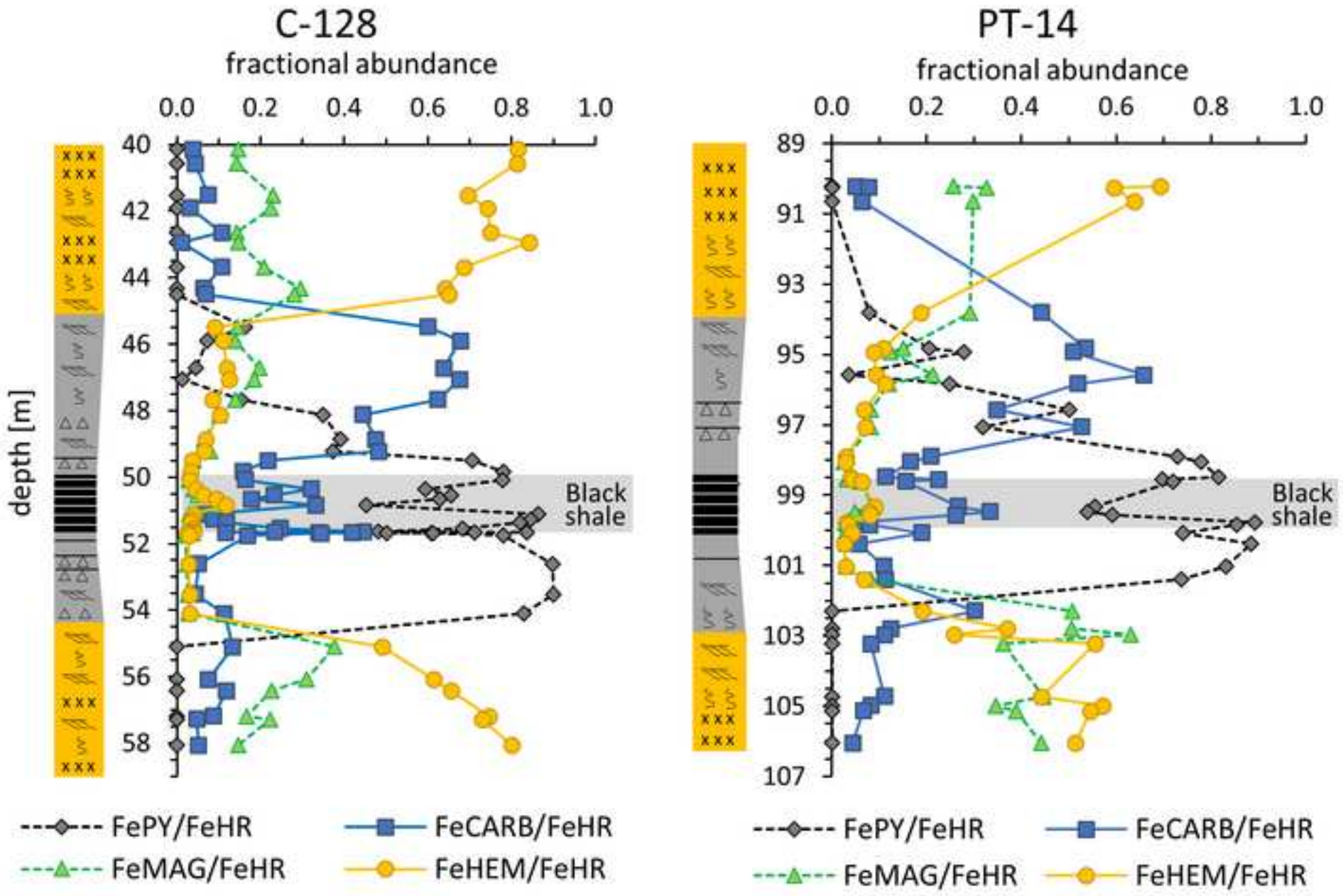

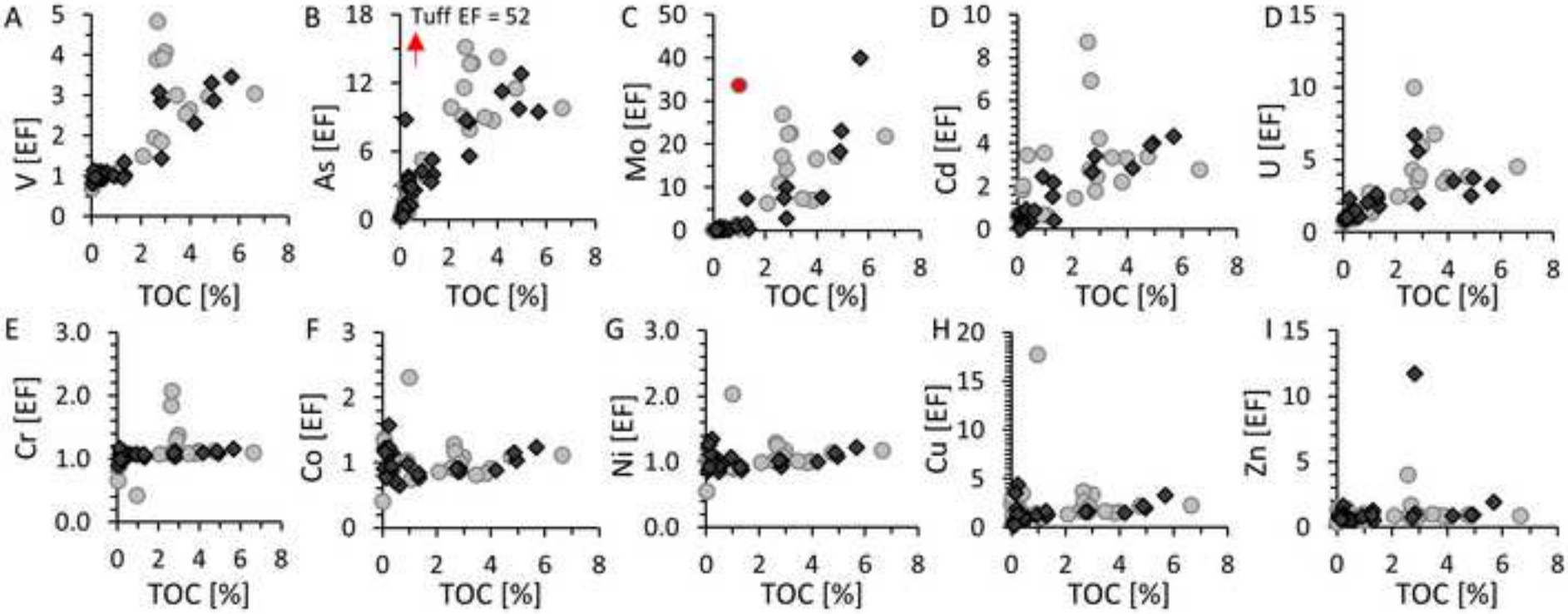

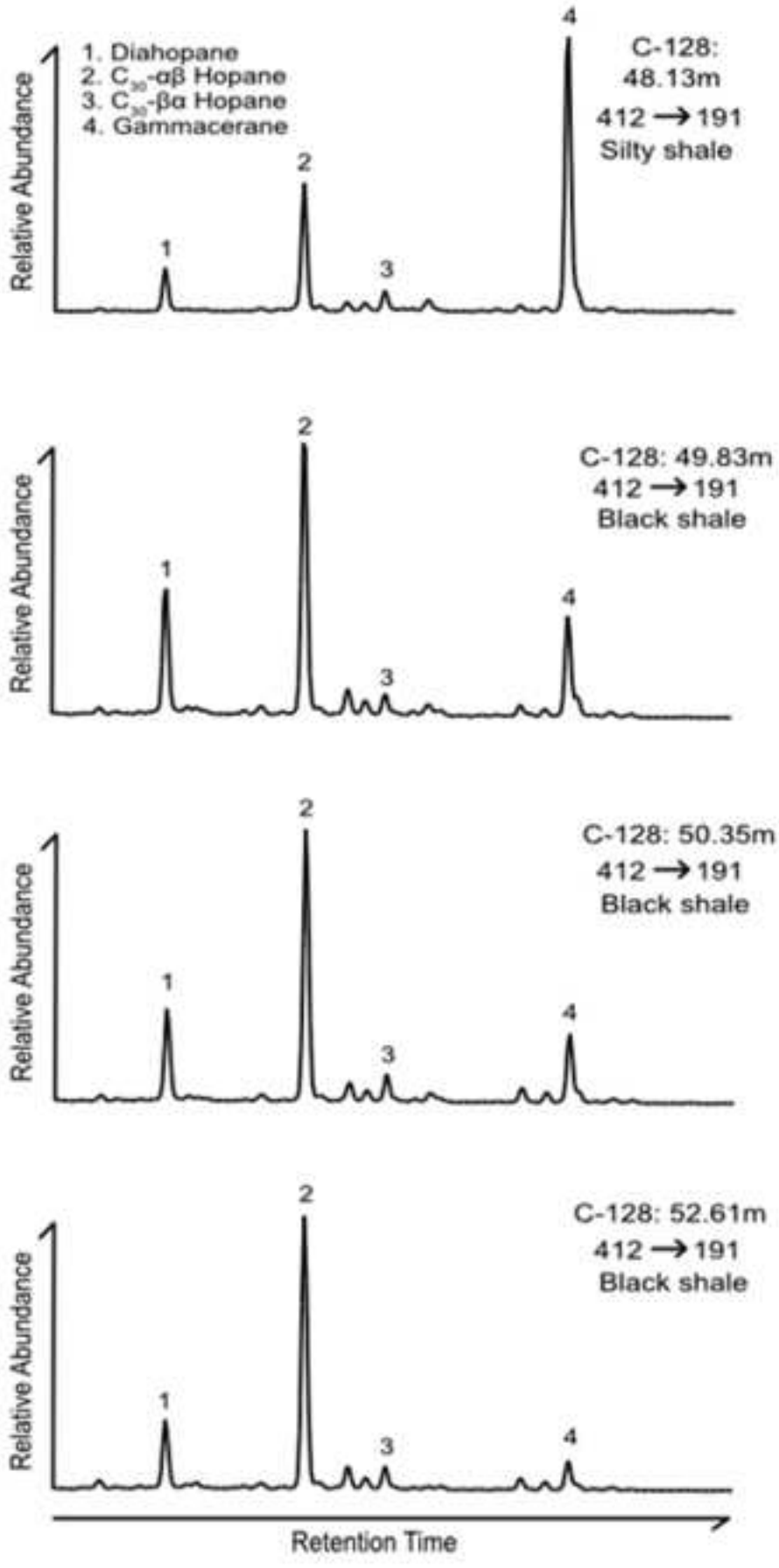

References

Abd-ElFattah, A.L.Y. and Wada, K., 1981. Adsorption of lead, copper, zinc, cobalt, and cadmium by soils that differ in cation- exchange materials. European Journal of Soil Science, 32(2): 271-283.

Abdulla, H.A., Burdige, D.J. and Komada, T., 2017. Accumulation of Deaminated Peptides in Anoxic Sediments of Santa Barbara Basin. Geochimica et Cosmochimica Acta: doi: 10.1016/j.gca.2017.11.021.

Anbar, A., Duan, Y., Lyons, T.W., Arnold, G.L., Kendall, B., Creaser, R.A., Kaufman, A.J., Gordon, G.W., Scott, C.T., Garvin, J. and Buick, R., 2007. A whiff of oxygen before the Great Oxidation Event? Science, 317(5846): 1903-1906.

Anderson, T.F. and Raiswell, R., 2004. Sources and mechanisms for the enrichment of highly reactive iron in euxinic Black Sea sediments. American Journal of Science, 304: 203-233.

Banta, A.B., Wei, J.H. and Welander, P.V., 2015. A distinct pathway for tetrahymanol synthesis in bacteria. Proceedings of the National Academy of Sciences, 112(44): 13478-13483.

Ben-Amotz, A. and Avron, M., 1983. On the factors which determine massive β-carotene accumulation in the halotolerant alga Dunaliella bardawil. Plant Physiology, 72(3): 593-597.

Berner, R.A. and Raiswell, R., 1983. Burial of organic carbon and pyrite sulfur in sediments over Phanerozoic time: a new theory. Geochimica et Cosmochimica Acta, 47(5): 855-862.

Berner, R.A. and Raiswell, R., 1984. C/S method for distinguishing freshwater from marine sedimentary rocks. Geology, 12(6): 365-368.

Blackburn, T.J., Olsen, P.E., Bowring, S.A., McLean, N.M., Kent, D.V., Puffer, J., McHone, G., Rasbury, E.T. and Et-Touhami, M., 2013. Zircon U-Pb geochronology links the end-Triassic extinction with the Central Atlantic Magmatic Province. Science, 340: 941-945.

Borowitzka, M.A., Borowitzka, L.J. and Kessly, D., 1990. Effects of salinity increase on carotenoid accumulation in the green alga Dunaliella salina. Journal of Applied Phycology, 2(2): 111-119.

Bruemmer, G.W., Gerth, J. and Tiller, K.G., 1988. Reaction kinetics of the adsorption and desorption of nickel, zinc and cadmium by goethite. I. Adsorption and diffusion of metals. European Journal of Soil Science, 38(1): 37-52.

Busigny, V., Lebeau, O., Ader, M., Krapež, B. and Bekker, A., 2013. Nitrogen cycle in the Late Archean ferruginous ocean. Chemical Geology, 362: 115-130.

Canfield, D.E., 1998. A new model for Proterozoic ocean chemistry. Nature, 396: 450-453.

Canfield, D.E., 2001. Biogeochemistry of sulfur isotopes. Reviews in Mineralogy and Geochemistry, 43(1): 607-636.

Canfield, D.E., Raiswell, R., Westrich, J.T., Reaves, C.M. and Berner, R.A., 1986. The use of chromium reduction in the analysis of reduced inorganic sulfur in sediments and shales. Chemical Geology, 54(1): 149-155.

Casas, I., de Pablo, J., Giménez, J., Torrero, M.E., Bruno, J., Cera, E., Finch, R.J. and Ewing, R.C., 1998. The role of pe, pH, and carbonate on the solubility of UO2 and uraninite under nominally reducing conditions. Geochimica et Cosmochimica Acta, 62: 2223-2231.

Chen, X., Ling, H.F., Vance, D., Shields-Zhou, G.A., Zhu, M., Poulton, S.W., Och, L., Jiang, S.-Y., Cremonese, L. and Archer, C., 2015. Rise to modern levels of ocean oxygenation coincided with the Cambrian radiation of animals. Nature communications, 6.

Clarkson, M.O., Poulton, S.W., Guilbaud, R. and Wood, R.A., 2014. Assessing the utility of Fe/Al and Fe-speciation to record water column redox conditions in carbonate-rich sediments. Chemical Geology, 382: 111-122.

Collister, J.W. and Hayes, J.M., 1973. A preliminary study of carbon and nitrogen isotopic biogeochemistry of lacustrine sedimentary rocks from the Green River Formation, Wyoming, Utah, and Colorado. In: M.L. Tuttle (Editor), Geochemical, biogeochemical, and sedimentological studies of the Green River formation, Wyoming, Utah, and Colorado. U.S. Geological Survey, Denver, CO.

Collister, J.W., Lichtfouse, E., Hieshima, G. and Hayes, J.M., 1990. Partial resolution of sources of n-alkanes in the saline portion of the Parachute Creek Member, Green River Formation (Piceance Creek Basin, Colorado). Organic Geochemistry, 21(6-7): 645-659.

Cox, G.M., Jarrett, A., Edwards, D., Crockford, P.W., Halverson, G.P., Collins, A.S., Poirier, A. and Li, Z.X., 2016. Basin redox and primary productivity within the Mesoproterozoic Roper Seaway. Chemical Geology, 440: 101-114.

Dahl, T.W., Hammarlund, E.U., Anbar, A.D., Bond, D.P., Gill, B.C., Gordon, G.W., Knoll, A.H., Nielsen, A.T., Schovsbo, N.H. and Canfield, D.E., 2010. Devonian rise in atmospheric oxygen correlated to the radiations of terrestrial plants and large predatory fish. Proceedings of the National Academy of Sciences, 107(42): 17911-17915.

Damsté, J.S.S., Kenig, F., Koopmans, M.P., Köster, J., Schouten, S., Hayes, J.M. and de Leeuw, J.W., 1995. Evidence for gammacerane as an indicator of water column stratification. Geochimica et Cosmochimica Acta, 59(9): 1895-1900.

De Grande, S.M.B., Aquino Neto, F.R. and Mello, M.R., 1993. Extended tricyclic terpanes in sediments and petroleums. Organic Geochemistry, 20(7): 1039-1047.

Eary, L.E. and Rai, D., 1987. Kinetics of chromium (III) oxidation to chromium (VI) by reaction with manganese dioxide. Environmental Science & Technology, 21(12): 1187-1193.

El Tabakh, M. and Schreiber, B.C., 1994. Lithologies and diagenesis of the lacustrine sediments of the Lockatong Formation (Upper Triassic) in the Newark rift basin. In: A.J. Lomando, B.C. Schreiber and P.M. Harris (Editors), Lacustrine reservoirs and depositional systems. Society for Sedimentary Geology, Denver, Colorado, pp. 239-295.

Fazeli, M.R., Tofighi, H., Samadi, N. and Jamalifar, H., 2006. Effects of salinity on β-carotene production by Dunaliella tertiolecta DCCBC26 isolated from the Urmia salt lake, north of Iran. Bioresource Technology, 97(18): 2453-2456.

Freudenthal, T., Wagner, T., Wenzhoefer, F., Zabel, M. and Wefer, G., 2001. Early diagenesis of organic matter from sediments of the eastern subtropical Atlantic: evidence from stable nitrogen and carbon isotopes. Geochimica et Cosmochimica Acta, 65(11): 1795-1808.

Garvin, J., Buick, R., Anbar, A.D., Arnold, G.L. and Kaufman, A.J., 2009. Isotopic evidence for an aerobic nitrogen cycle in the latest Archean. Science, 323: 1045-1048.

Gierlowski-Kordesch, E. and Rust, B.R., 1994. The Jurassic East Berlin Formation, Hartford Basin, Newark Supergroup (Connecticut and Massachusetts): A Saline Lake Playa Alluvial Plain System. Sedimentology and Geochemistry of Modern and Ancient Saline Lakes, SEPM Special Publication, 50: 249-265.

Gilleaudeau, G.J. and Kah, L.C., 2015. Heterogeneous redox conditions and a shallow chemocline in the Mesoproterozoic ocean: evidence from carbon–sulfur–iron relationships. Precambrian Research, 257: 94-108.

Godfrey, L.V. and Falkowski, P.G., 2009. The cycling and redox state of nitrogen in the Archaean ocean. Nature Geoscience, 2: 725-729.

Godfrey, L.V. and Glass, J.B., 2011. The geochemical record of the ancient nitrogen cycle, nitrogen isotopes, and metal cofactors. Methods in Enzymology, 486: 483-506.

Gold, D.A., Grabenstatter, J., de Mendoza, A., Riesgo, A., Ruiz-Trillo, I. and Summons, R.E., 2016. Sterol and genomic analyses validate the sponge biomarker hypothesis. Proceedings of the National Academy of Sciences, 113(10): 2684-2689.

Grice, K., Schouten, S., Peters, K.E. and Damsté, J.S.S., 1998. Molecular isotopic characterisation of hydrocarbon biomarkers in Palaeocene–Eocene evaporitic, lacustrine source rocks from the Jianghan Basin, China. Organic Geochemistry, 29(5): 1745-1764.

Gudbrandsson, S., Wolff-Boenisch, D., Gislason, S.R. and Oelkers, E.H., 2011. An experimental study of crystalline basalt dissolution from $2 \leq pH \leq 11$ and temperatures from 5 to 75 °C. Geochimica et Cosmochimica Acta, 75: 5496-5509.

Guo, W., Mosenfelder, J.L., Goddard, W.A. and Eiler, J.M., 2009. Isotopic fractionations associated with phosphoric acid digestion of carbonate minerals: insights from first-principles theoretical modeling and clumped isotope measurements. Geochimica et Cosmochimica Acta, 73(24): 7203-7225.

Haendel, D., Muehle, K., Nitzsche, H.-M., Stiehl, G. and Wand, U., 1986. Isotopic variations of the fixed nitrogen in metamorphic rocks. Geochimica et Cosmochimica Acta, 50: 749-758.

Halevy, I. and Bachan, A., 2017. The geologic history of seawater pH. Science, 355: 1069-1071.

Hardisty, D.S., Lu, Z., Bekker, A., Diamond, C.W., Gill, B.C., Jiang, G., Kah, L.C., Knoll, A.H., Loyd, S.J., Osburn, M.R. and Planavsky, N.J., 2017. Perspectives on Proterozoic surface ocean redox from iodine contents in ancient and recent carbonate. Earth and Planetary Science Letters, 463: 159-170.

Harrison, W.J., Pevear, D.R. and Lindahl, P.C., 1973. Trace elements in pyrites of the Green River Formation oil shales, Wyoming, Utah, and Colorado. In: M.L. Tuttle (Editor), Geochemical, biogeochemical, and sedimentological studies of the Green River formation, Wyoming, Utah, and Colorado. U.S. Geological Survey, Denver, CO.

Hatcher, P.G. and Romankiw, L.A., 1985. Nuclear magnetic resonance studies of organic-matter-rich sedimentary rocks of some early Mesozoic basins of the eastern United States. In: G.R. Robinson and A.J. Froelich (Editors), Proceedings of the second US Geological Survey workshop in the early Mesozoic basins of the eastern United States, pp. 65-70.

Hay, W.W., Behensky Jr, J.F., Barron, E.J. and Sloan II., J.L., 1982. Late Triassic-Liassic Paleoclimatology of the proto-central North Atlantic rift system. Paleogeography, Paleoclimatology, Palaeoecology, 40: 13-30.

Hebting, Y., Schaeffer, P., Behrens, A., Adam, P., Schmitt, G., Schneckenburger, P., Bernasconi, S.M. and Albrecht, P., 2006. Biomarker evidence for a major preservation pathway of sedimentary organic carbon. Science, 312(5780): 1627-1631.

Helz, G.R., Bura-Nakic, E., Mikac, N. and Ciglenecki, I., 2011. New model for molybdenum behavior in euxinic waters. Chemical Geology, 284: 323-332.

Horsfield, B., Curry, D.J., Bohacs, K., Littke, R., Rullkötter, J., Schenk, H.J., Radke, M., Schaefer, R.G., Carroll, A.R., Isaksen, G. and Witte, E.G., 1994. Organic geochemistry of freshwater and alkaline lacustrine sediments in the Green River Formation of the Washakie Basin, Wyoming, USA. Organic Geochemistry, 22(3-5): 415-440.

Horton, T.W., Defliese, W.F., Tripati, A.K. and Oze, C., 2016. Evaporation induced ^{18}O and ^{13}C enrichment in lake systems: a global perspective on hydrologic balance effects. Quaternary Science Reviews, 131: 365-379.

Isson, T.T. and Planavsky, N.J., 2018. Reverse weathering as a long-term stabilizer of marine pH and planetary climate. Nature, 560(7719): 471-475.

Jellison, R., Miller, L.G., Melack, J.M. and Dana, G.L., 1993. Meromixis in hypersaline Mono Lake, California. II: Nitrogen fluxes. Limnology and Oceanography, 38(5): 1020-1039.

Jiamo, F., Guoying, S., Jiayou, X., Eglinton, G., Gowar, A.P., Rongfen, J., Shanfa, F. and Pingan, P., 1990. Application of biological markers in the assessment of paleoenvironments of Chinese non-marine sediments. Organic Geochemistry, 16(4-6): 769-779.

Kaufman, A.J., Johnston, D.T., Farquhar, J., Masterson, A.L., Lyons, T.W., Bates, S., Anbar, A., Arnold, G.L., Garvin, J. and Buick, R., 2007. Late Archean biospheric oxygenation and atmospheric evolution. Science, 317: 1900-1903.

Kendall, B., Creaser, R.A., Reinhard, C.T., Lyons, T.W. and Anbar, A.D., 2015. Transient episodes of mild environmental oxygenation and oxidative continental weathering during the late Archean. Science Advances, 1(10): DOI: 10.1126/sciadv.1500777

Kent, D.V. and Tauxe, L., 2005. Corrected Late Triassic latitudes for continents adjacent to the North Atlantic. Science, 307(5707): 240-244.

Kipp, M.A., Stüeken, E.E., Bekker, A. and Buick, R., 2017. Selenium isotopes record extensive marine suboxia during the Great Oxidation Event. Proceedings of the National Academy of Sciences, 114(5): 875-880.

Koehler, M.C., Stüeken, E.E., Kipp, M.A., Buick, R. and Knoll, A.H., 2017. Spatial and temporal trends in Precambrian nitrogen cycling: a Mesoproterozoic offshore nitrate minimum. Geochimica et Cosmochimica Acta, 198: 315-337.

Kruge, M.A., Hubert, J.F., Bensley, D.F., Crelling, J.C., Akes, R.J. and Meriney, P.E., 1989. Organic geochemistry of a Lower Jurassic synrift lacustrine sequence, Hartford basin, Connecticut, USA. Advances in Organic Geochemistry, 16(4-6): 689-701.

Lalonde, S.V. and Konhauser, K.O., 2015. Benthic perspective on Earth's oldest evidence for oxygenic photosynthesis. Proceedings of the National Academy of Sciences, 112(4): 995-1000.

Lehman, M.R., Bernasconi, S.M., Barbieri, A. and McKenzie, J.A., 2002. Preservation of organic matter and alteration of its carbon and nitrogen isotope composition during simulated and in situ early sedimentary diagenesis. Geochimica et Cosmochimica Acta, 66(20): 3573-3584.

Lent, R.M., Lyons, W.B., Showers, W.J. and Johannesson, K.H., 1995. Late Holocene paleoclimatic and paleobiologic records from sediments of Devils Lake, North Dakota. Journal of Paleolimnology, 13(3): 193-207.

Leventhal, J.S., 1983. An interpretation of carbon and sulfur relationships in Black Sea sediments as indicators of environments of deposition. Geochimica et Cosmochimica Acta, 47(1): 133-137.

Lewis, A.E., 2010. Review of metal sulphide precipitation. Hydrometallurgy, 104: 222-234.

Li, L., Sherwood Lollar, B., Li, H., Wortmann, U.G. and Lacrampe-Couloume, G., 2012. Ammonium stability and nitrogen isotope fractionations for NH_4^+-$NH_{3(aq)}$-$NH_{3(gas)}$ systems at 20-70^{o}C and pH of 2-13: applications to habitability and nitrogen cycling in low-temperature hydrothermal systems. Geochimica et Cosmochimica Acta, 84: 280-296.

Lyons, T.W., 1997. Sulfur isotopic trends and pathways of iron sulfide formation in upper Holocene sediments of the anoxic Black Sea. Geochimica et Cosmochimica Acta, 61(16): 3367-3382.

Lyons, T.W., Luepke, J.J., Schreiber, M.E. and Zieg, G.A., 2000. Sulfur geochemical constraints on Mesoproterozoic restricted marine deposition: lower Belt Supergroup, northwestern United States. Geochimica et Cosmochimica Acta, 64(3): 427-437.

Lyons, T.W. and Severmann, S., 2006. A critical look at iron paleoredox proxies: new insights from modern euxinic marine basins. Geochimica et Cosmochimica Acta, 70(23): 5698-5722.

Lyons, T.W., Werne, J.P., Hollander, D.J. and Murray, R.W., 2003. Contrasting sulfur geochemistry and Fe/Al and Mo/Al ratios across the last oxic-to-anoxic transition in the Cariaco Basin, Venezuela. Chemical Geology, 195(1): 131-157.

Maher, K., Bargar, J.R. and Brown Jr., G.E., 2013. Environmental speciation of actinides. Inorganic Chemistry, 52: 3510-3532.

Malinconico, M.A., 2002. Lacustrine organic sedimentation, organic metamorphism and thermal history of selected Early Mesozoic Newark Supergroup basins, Columbia University, New York, 419 pp.

McGroddy, M.E., Daufresne, T. and Hedin, L.O., 2004. Scaling of C: N: P stoichiometry in forests worldwide: Implications of terrestrial redfield- type ratios. Ecology, 85(9): 2390-2401.

McLauchlan, K.K., Williams, J.J., Craine, J.M. and Jeffers, E.S., 2013. Changes in global nitrogen cycling during the Holocene epoch. Nature, 495(7441): 352-355.

Menzel, P., Gaye, B., Wiesner, M.G., Prasad, S., Stebich, M., Krishna Das, B., Anoop, A., Riedel, N. and Basavaiah, N., 2013. Influence of bottom water anoxia on nitroen isotopic ratios and amino acid contributions of recent sediments from small eutrophic Lonar Lake, central India. Limnology and Oceanography, 58(3): 1061-1074.

Moldowan, J.M., Fago, F.J., Lee, C.Y., Jacobson, S.R., Watt, D.S., Slougui, N.-E., Jeganathan, A. and Young, D.C., 1990. Sedimentary 24-n-propylcholestanes, molecular fossils diagnostic of marine algae. Science, 247: 309-312.

Morgan, B. and Lahav, O., 2007. The effect of pH on the kinetics of spontaneous Fe(II) oxidation by O_2 in aqueous solution–basic principles and a simple heuristic description. Chemosphere, 68(11): 2080-2084.

Müller, P.J., 1977. CN ratios in Pacific deep-sea sediments: Effect of inorganic ammonium and organic nitrogen compounds sorbed by clays. Geochimica et Cosmochimica Acta, 41(6): 765-776.

Och, L.M. and Shields-Zhou, G.A., 2012. The Neoproterozoic oxygenation event: environmental perturbations and biogeochemical cycling. Earth-Science Reviews, 110(1): 26-57.

Olsen, P.E., 1986. A 40-million-year lake record of early Mesozoic climatic forcing. Science, 234(842-848).

Olsen, P.E., 1988a. Continuity of strata in the Newark and Hartford Basins of the Newark Supergroup. U.S. Geological Survey Bulletin, 1776: 6-18.

Olsen, P.E., 1988b. Paleoecology and paleoenvironments of the continental early Mesozoic Newark Supergroup of eastern North America. In: W. Manspeizer (Editor), Triassic-Jurassic rifting and the openning of the Atlantic ocean. Elsevier, Amsterdam, pp. 185-230.

Olsen, P.E., 1990. Tectonic, climatic, and biotic modulation of lacustrine ecosystems: examples from the Newark Supergroup of eastern North America. In: B. Katz (Editor), Lacustrine Basin Exploration: Case Studies and Modern Analogs. American Association Petroleum Geologists Memoir American Association Petroleum Geologists, pp. 209-224.

Olsen, P.E., 1997. Stratigraphic record of the early Mesozoic breakup of Pangea in the Laurasia-Gondwana rift system. Annual Reviews in Earth and Planetary Sciences, 25: 337-401.

Olsen, P.E., 2011. Fossil Great Lakes of the Newark Supergroup – 30 Years Later. In: A.I. Benimoff (Editor), Field Trip Guidebook. New York State Geological Association, New York, pp. 101-162.

Olsen, P.E., 2012. Air-fall ashes of the CAMP from eastern North America and Morocco, GSA Northeastern Section, annual meeting. Geological Society of America, Hartford, Connecticut, pp. 56.

Olsen, P.E. and Kent, D.V., 1996. Milankovitch climate forcing in the tropics of Pangaea during the Late Triassic. Paleogeography, Paleoclimatology, Palaeoecology, 122: 1-26.

Olsen, P.E., Kent, D.V., Cornet, B., Witte, W.K. and Schlische, R.W., 1996a. High-resolution stratigraphy of the Newark rift basin (early Mesozoic, eastern North America). Geological Society of America Bulletin, 108(1): 40-77.

Olsen, P.E., Schlische, R.W. and Fedosh, M.S., 1996b. 580 kyr duration of the Early Jurassic flood basalt event in eastern North America estimated using Milankovitch cyclostratigraphy. In: M. Morales (Editor), The continental Jurassic. Museum of Northern Arizona Bulletin, pp. 11-22.

Olsen, P.E., Whiteside, J.H. and Huber, P., 2003. Causes and consequences of the Triassic-Jurassic mass extinction as seen from the Hartford basin. In: J.B. Brady and J.T. Cheney (Editors), Guidebook for Field Trips in the Five College Region. 95th New England Intercollegiate Geological Conference, Department of Geology, Smith College, Northampton, Massachusetts, pp. 1-41.

Partin, C.A., Bekker, A., Planavsky, N.J. and Lyons, T.W., 2015. Euxinic conditions recorded in the ca. 1.93 Ga Bravo Lake Formation, Nunavut (Canada): Implications for oceanic redox evolution. Chemical Geology, 417: 148-162.

Poulton, S.W. and Canfield, D.E., 2005. Development of a sequential extraction procedure for iron: implications for iron partitioning in continentally derived particulates. Chemical Geology, 214(3): 209-221.

Poulton, S.W. and Canfield, D.E., 2011. Ferruginous conditions: a dominant feature of the ocean through Earth's history. Elements, 7: 107-112.

Poulton, S.W., Fralick, P.W. and Canfield, D.E., 2010. Spatial variability in oceanic redox structure 1.8 billion years ago. Nature Geoscience, 3: 486-490.

Poulton, S.W. and Raiswell, R., 2002. The low-temperature geochemical cycle of iron: from continental fluxes to marine sediment deposition. American Journal of Science, 302(9): 774-805.

Pratt, L.M., 1989. Deposition, diagenesis, and maturation of organic matter in rift-basin lacustrine shales of Triassic-Jurassic Newark Supergroup, AAPG annual convention. American Association of Petroleum Geology, San Antonio, Texas, pp. CONF-890404.

Pratt, L.M., Vuletich, A.K. and Daws, T.A., 1985. Geochemical and isotopic characterization of organic matter in rocks of the Newark Supergroup. In: G.R. Robinson and A.J. Froelich (Editors), Proceedings of the second US Geological Survey workshop on the early Mesozoic basins of the eastern United States. US Geological Survey, pp. 74-78.

Raiswell, R., 2011. Iron transport from the continents to the open ocean: The aging–rejuvenation cycle. Elements, 7(2): 101-106.

Raiswell, R. and Berner, R.A., 1987. Organic carbon losses during burial and thermal maturation of normal marine shales. Geology, 15(9): 853-856.

Raiswell, R. and Canfield, D.E., 1998. Sources of iron for pyrite formation in marine sediments. American Journal of Science, 298(3): 219-245.

Reich, P.B. and Oleksyn, J., 2004. Global patterns of plant leaf N and P in relation to temperature and latitude. Proceedings of the National Academy of Sciences, 101(30): 11001-11006.

Reinhard, C.T., Lyons, T.W., Rouxel, O., Asael, D., Dauphas, N. and Kump, L.R., 2013. Iron Speciation and Isotope Perspectives on Palaeoproterozoic Water Column Chemistry. In: L.R. Kump, A.B. Kuznetsov, I.M. Gorokhov, V.A. Melezhik, J. Farkaš, R. Chakrabarti, S.B. Jacobsen, C.T. Reinhard, T.W. Lyons, O. Rouxel, D. Asael, N. Dauphas, M. van Zuilen, R. Schoenberg, F.L.H. Tissot, J.L. Hannah and H.J. Stein (Editors), Reading the Archive of Earth's Oxygenation. Springer Berlin, pp. 1483-1492.

Reinhard, C.T., Raiswell, R., Scott, C.T., Anbar, A. and Lyons, T.W., 2009. A late Archean sulfidic sea stimulated by early oxidative weathering of the continents. Science, 326: 713-716.

Robinson, R.S., Kienast, M., Albuquerque, A.L., Altabet, M., Contreras, S., De Pol Holz, R., Dubois, N., Francois, R., Galbraith, E., Shu, T.-C., Ivanochko, T., Jaccard, S., Kao, S.-J., Kiefer, T., Kienast, S., Lehmann, M., Martinez, P., McCarthy, M., Moebius, J., Pedersen, T., Quan, T.M., Ryabenko, E., Schmittner, A., Schneider, R., Schneider-Mor, A., Shigemitsu, M., Sinclair, D., Somes, C., Studer, A., Thunell, R. and Yang, J.-Y., 2012. A review of nitrogen isotopic alteration in marine sediments. Paleoceanography, 27(PA4203): doi: 10.1029/2012PA002321.

Rohrssen, M., Love, G.D., Fischer, W., Finnegan, S. and Fike, D.A., 2013. Lipid biomarkers record fundamental changes in the microbial community structure of tropical seas during the Late Ordovician Hirnantian glaciation. Geology, 41: 127-130.

Ruble, T.E., Bakel, A.J. and Philp, R.P., 1994. Compound specific isotopic variability in Uinta Basin native bitumens: paleoenvironmental implications. Organic Geochemistry, 21(6-7): 661-671.

Rudnick, R.L. and Gao, S., 2014. Composition of the continental crust. Treatise on Geochemistry, 4: 1-51.

Sahoo, S.K., Planavsky, N.J., Kendall, B., Wang, X., Shi, X., Scott, C., Anbar, A.D., Lyons, T.W. and Jiang, G., 2012. Ocean oxygenation in the wake of the Marinoan glaciation. Nature, 489: 546-549.

Schidlowski, M., 1987. Application of stable carbon isotopes to early biochemical evolution on Earth. Annual Review of Earth and Planetary Sciences, 15: 47-72.

Schlische, R.W., 1990. Structural and stratigraphic development of the Newark extensional basin, eastern North America; evidence for the growth of the basin and its bounding structures. Geological Society of America Bulletin, 104: 1246-1263.

Schmidt, F., Koch, B.P., Elvert, M., Schmidt, G., Witt, M. and Hinrichs, K.U., 2011. Diagenetic transformation of dissolved organic nitrogen compounds under contrasting sedimentary redox conditions in the Black Sea. Environmental Science & Technology, 45(12): 5223-5229.

Schroeder, P.A. and McLain, A.A., 1998. Illite-smectites and the influence of burial diagenesis on the geochemical cycling of nitrogen. Clay Minerals, 33(4): 539-546.

Scott, C. and Lyons, T.W., 2012. Contrasting molybdenum cycling and isotopic properties in euxinic versus non-euxinic sediments and sedimentary rocks: refining the paleoproxies. Chemical Geology, 324: 19-27.

Scott, C., Lyons, T.W., Bekker, A., Shen, Y., Poulton, S.W., Chu, X. and Anbar, A.D., 2008. Tracing the stepwise oxygenation of the Proterozoic ocean. Nature, 452: 456-459.

Scott, C., Planavsky, N.J., Dupont, C.L., Kendall, B., Gill, B.C., Robbins, L.J., Husband, K.F., Arnold, G.L., Wing, B., Poulton, S.W., Bekker, A., Anbar, A., Konhauser, K. and Lyons, T.W., 2012. Bioavailability of zinc in marine systems through time. Nature Geoscience, 6: 125-128.

Severmann, S., Lyons, T.W., Anbar, A., McManus, J. and Gordon, G., 2008. Modern iron isotope perspective on the benthic iron shuttle and the redox evolution of ancient oceans. Geology, 36: 487-490.

Sim, M.S., Bosak, T. and Ono, S., 2011. Large sulfur isotope fractionation does not require disproportionation. Science, 333(6038): 74-77.

Sperling, E.A., Wolock, C.J., Morgan, A.S., Gill, B.C., Kunzmann, M., Halverson, G.P., Macdonald, F.A., Knoll, A.H. and Johnston, D.T., 2015. Statistical analysis of iron geochemical data suggests limited late Proterozoic oxygenation. Nature, 523: 451-454.

Spiker, E.C., 1985. Stable-isotope characterization of organic matter in the early Mesozoic basins of the eastern United States. In: G.R. Robinson and A.J. Froelich (Editors), Proceedings of the second US Geological Survey workshop on the early Mesozoic basins of the eastern United States. US Geological Survey, pp. 70-73.

Spiker, E.C., Kotra, R.K., Hatcher, P.G., Goffried, R.M., Horan, M.F. and Olsen, P.E., 1988. Source of kerogen in black shales from the Hartford and Newark basins, eastern United States. In: A.J. Froelich and G.R. Robinson (Editors), Studies of the Early Mesozoic Basins of the Eastern United States: A Summary of Current Research on Early Mesozoic Sedimentary and Igneous Rocks and Related Mineral Resources. US Geological Survey Bulletin. US Geological Survey, pp. 63-68.

Stüeken, E.E., 2013. A test of the nitrogen-limitation hypothesis for retarded eukaryote radiation: nitrogen isotopes across a Mesoproterozoic basinal profile. Geochimica et Cosmochimica Acta, 120: 121-139.

Stüeken, E.E., Buick, R. and Anbar, A.D., 2015a. Selenium isotopes support free O_2 in the latest Archean. Geology, 43(3): 259-262.

Stüeken, E.E., Buick, R., Guy, B.M. and Koehler, M.C., 2015b. Isotopic evidence for biological nitrogen fixation by Mo-nitrogenase at 3.2 Gyr. Nature, 520: 666-669.

Stüeken, E.E., Buick, R. and Schauer, A.J., 2015c. Nitrogen isotope evidence for alkaline lakes on late Archean continents. Earth and Planetary Science Letters, 411: 1-10.

Stüeken, E.E., Catling, D.C. and Buick, R., 2012. Contributions to late Archaean sulphur cycling by life on land. Nature Geoscience, 5: 722-725.

Stumm, W. and Morgan, J.J., 1996. Aquatic Chemistry. John Wiley & Sons, Inc.

Suchecki, R.K., Hubert, J.F. and Birney de Wet, C.C., 1988. Isotopic imprint of climate and hydrogeochemistry on terrestrial strata of the Triassic-Liassic Hartford and Fundy rift basins. Journal of Sedimentary Petrology, 58(5): 801-811.

Summons, R.E., Hope, J.M., Swart, R. and Walter, M.R., 2008. Origin of Nama Basin bitumen seeps: Petroleum derived from a Permian lacustrine source rock traversing southwestern Gondwana. Organic Geochemistry, 39(5): 589-607.

Tack, F.M., Callewaert, O.W.J.J. and Verloo, M.G., 1996. Metal solubility as a function of pH in a contaminated, dredged sediment affected by oxidation. Environmental Pollution, 91(2): 199-208.

Talbot, M.R., 1990. A review of the palaeohydrological interpretation of carbon and oxygen isotopic ratios in primary lacustrine carbonates. Chemical Geology, 80(4): 261-279.

Talbot, M.R. and Johannessen, T., 1992. A high resolution palaeoclimatic record for the last 27,500 years in tropical west Africa from the carbon and nitroen isotopic composition of lacustrine organic matter. Earth and Planetary Science Letters, 110: 23-37.

Tesdal, J.E., Galbraith, E.D. and Kienast, M., 2013. Nitrogen isotopes in bulk marine sediment: linking seafloor observations with subseafloor records. Biogeosciences, 10(1): 101-118.

Tiller, K.G., Gerth, J. and Brümmer, G., 1984. The sorption of Cd, Zn and Ni by soil clay fractions: procedures for partition of bound forms and their interpretation. Geoderma, 34(1): 1-16.

Van Houten, F.B., 1962. Cyclic sedimentation and the origin of analcime-rich upper Triassic Lockatong Formation, west-central New Jersey adn adjacent Pennsylvania. American Journal of Science, 260: 561-571.

Van Houten, F.B., 1965. Composition of Triassic Lockatong and associated formations of Newark Group, central New Jersey and adjacent Pennsylvania American Journal of Science, 263: 825-863.

Weems, R.E. and Olsen, P.E., 1997. Synthesis and revision of groups within the Newark Supergroup. Geological Society of America Bulletin, 109: 195-209.

Whiteside, J.H., Olsen, P.E., Eglinton, T.I., Cornet, B., McDonald, N. and Huber, P., 2011. Pangean great lake paleoecology on the cusp of the end-Triassic extinction. Paleogeography, Paleoclimatology, Palaeoecology, 301: 1-17.

Whiteside, J.H., Olsen, P.E., Kent, D.V., Fowell, S.J. and Et-Touhami, M., 2007. Synchrony between the CAMP and the Triassic-Jurassic mass-extinction event? Palaeogeography, Palaeoclimatology, and Palaeoecology, 244(1-4): 345-367.

Wijsman, J.W., Middleburg, J.J. and Heip, C.H., 2001. Reactive iroin in Black Sea sediments: implications for iron cycling. Marine Geology, 172(3-4): 167-180.

Witte, W.K., Kent, D.V. and Olsen, P.E., 1991. Magnetostratigraphy and paleomagnetic poles from Late Triassic-earliest Jurassic strata of the Newark basin. Geological Society of America Bulletin, 103: 1648-1662.

Zachara, J.M., Cowan, C.E. and Resch, C.T., 1991. Sorption of divalent metals on calcite. Geochimica et Cosmochimica Acta, 55(6): 1549-1562.

Zayed, A.M. and Terry, N., 2003. Chromium in the environment: factors affecting biological remediation. Plant and Soil, 249: 139-156.

Zerkle, A., House, C.H. and Brantley, S.L., 2005. Biogeochemical signatures through time as inferred from whole microbial genomes. American Journal of Science, 305: 467-502.

Zerkle, A.L., Poulton, S.W., Newton, R.J., Mettam, C., Claire, M.W., Bekker, A. and Junium, C.K., 2017. Onset of the aerobic nitrogen cycle during the Great Oxidation Event. Nature, 542: 465-467.

Zinabu, G.M. and Pearce, N.J., 2003. Concentrations of heavy metals and related trace elements in some Ethiopian rift-valley lakes and their in-flows. Hydrobiologia, 492(1-3): 171-178.

Table 1: Organic carbon, total nitrogen and carbonate carbon and oxygen data

sample ID	Pos. [m]	TOC [%]	$\delta^{13}C_{org}$ [‰]	C/N [at]	TN [%]	$\delta^{15}N$ [‰]	$\delta^{13}C_{carb}$ [‰]	$\delta^{18}O_{carb}$ [‰]	$MgCO_3$ [%]	$CaCO_3$ [%]	Ca/Mg [at]
core C-128:											
C128_143.3	43.68	0.02	-24.25	3.63	0.01	3.03	-6.62	-3.67	1.12	9.82	7.88
C128_145.4	44.32	0.05	-24.26	2.84	0.02	4.58	-2.16	1.45	1.85	3.89	1.90
C128_146.0	44.50	0.07	-25.42	2.54	0.03	4.60	-1.82	1.13	1.36	2.93	1.94
C128_149.2	45.48	0.40	-26.50	10.68	0.04	5.82	-1.57	1.78	5.45	9.35	1.55
C128_150.6	45.90	0.32	-26.62	7.06	0.05	5.02	-1.14	1.88	3.89	6.47	1.50
C128_153.3	46.73	0.18	-26.01	5.86	0.04	4.12	-0.70	1.15	3.23	5.11	1.43
C128_154.4	47.06	0.19	-26.19	5.53	0.04	4.39	-0.18	1.77	3.67	6.04	1.48
C128_156.4	47.67	0.20	-26.54	7.31	0.03	3.91	-0.92	-0.69	2.47	6.74	2.46
C128_157.9	48.13	0.35	-26.38	8.41	0.05	5.53	0.06	1.94	3.92	6.27	1.45
C128_160.3	48.86	0.32	-27.25	7.71	0.05	4.99	0.52	1.91	4.19	8.19	1.76
C128_161.5	49.23	0.31	-27.29	8.01	0.04	5.00	0.20	1.10	4.20	6.83	1.47
C128_162.4	49.50	0.36	-27.39	9.19	0.05	4.94	0.44	1.25	6.13	7.03	1.03
C128_163.5	49.83	1.06	-30.10	24.33	0.05	6.57	1.10	2.24	6.35	9.56	1.36
C128_164.3	50.08	0.92	-30.22	24.27	0.04	5.94	0.66	1.36	5.85	8.10	1.25
C128_165.2	50.35	2.57	-29.67	40.18	0.07	10.53	-0.68	-0.64	10.62	14.47	1.23
C128_165.8	50.54	4.75	-29.78	45.36	0.12	12.66	-1.98	-2.16	8.47	11.96	1.28
C128_166.2	50.66	2.83	-29.88	41.61	0.08	11.54	-1.77	-0.82	10.12	13.99	1.25
C128_166.8	50.84	6.64	-29.71	45.31	0.17	14.47	-3.49	-3.73	9.06	16.30	1.62
C128_167.7	51.11	3.98	-29.25	39.89	0.12	9.18	-2.50	-1.73	4.19	6.48	1.40
C128_168.2	51.27	2.08	-29.65	36.04	0.07	6.20	-1.77	-0.67	3.59	7.33	1.84
C128_168.5	51.36	3.82	-28.99	40.91	0.11	7.38	-2.93	-2.45	4.76	9.38	1.78
C128_169.1	51.54	3.46	-29.29	46.66	0.09	6.92	-3.63	-3.41	7.97	14.66	1.66
C128TUFF-6	51.64	2.98	-31.00	45.26	0.08	8.34	-4.85	0.01	24.41	31.06	1.15
C128TUFF-5	51.66	2.64	-31.13	39.93	0.07	8.18	-4.79	-0.03	24.88	30.76	1.12
C128TUFF-4	51.66	0.98	-31.76	20.71	0.04	5.13	-4.71	1.13	26.02	32.19	1.12
C128TUFF-3	51.67	2.68	-31.13	42.37	0.07	8.07	-11.41	-4.18	1.93	12.57	5.88
C128TUFF-2	51.68	2.88	-31.11	44.44	0.07	8.88	-4.84	0.56	19.06	23.08	1.09
C128TUFF-1	51.69	3.02	-30.92	43.58	0.08	8.62	-4.47	0.46	25.69	31.95	1.12
C128_169.8	51.76	2.45	-30.05	39.41	0.07	6.84	-3.20	-1.15	10.49	14.95	1.29
C128_172.6	52.61	1.04	-30.21	22.70	0.05	5.90	-2.35	0.37	1.54	2.50	1.47
C128_175.6	53.52	0.30	-28.83	7.62	0.05	4.84	-2.26	0.20	1.58	2.16	1.24
C128_177.5	54.10	1.86	-30.44	29.74	0.07	7.29	-3.51	1.16	6.93	8.56	1.12
C128_180.8	55.11	0.10	-26.48	11.51	0.01	2.56			0.40	0.81	1.83
core PT-14:											
PT14_296'1''	90.25	0.06	-24.64	3.00	0.02	5.27			3.00	3.05	0.92
PT14_297'5''	90.65	0.09	-25.55	2.24	0.05	5.61			2.26	2.41	0.97
PT14_307'5''	93.80	0.23	-25.90	11.13	0.02	5.11			1.66	1.79	0.98
PT14_311'1''	94.82	0.29	-26.18	7.31	0.05	6.15			3.42	3.70	0.97
PT14_311'5''	94.92	0.20	-26.11	6.24	0.04	4.59	-0.38	2.14	3.00	3.77	1.14

PT14_313'7''	95.58	0.46	-26.03	10.22	0.05	7.02	-0.52	1.65	4.03	4.80	1.08
PT14_314'5''	95.83	0.35	-26.89	11.36	0.04	5.01	-0.31	1.91	3.90	4.68	1.08
PT14_316'10''	96.57	0.35	-26.87	8.04	0.05	5.66	-0.35	1.70	4.28	5.45	1.15
PT14_318'5''	97.05	0.32	-26.89	7.55	0.05	4.92	-0.15	1.75	4.25	4.76	1.01
PT14_321'2''	97.89	0.61	-29.15	13.63	0.05	5.52	0.17	1.79	4.60	4.80	0.94
PT14_321'8''	98.04	1.35	-29.83	34.08	0.05	5.76	0.54	1.82	6.95	8.82	1.15
PT14_323'1''	98.48	0.46	-27.63	10.94	0.05	5.09	0.89	2.02	4.72	4.50	0.86
PT14_323'4''	98.55	2.83	-30.24	45.13	0.07	9.18	0.78	1.73	8.27	10.14	1.11
PT14_323'6''	98.60	1.31	-29.91	33.51	0.05	6.88	-0.26	0.76	7.63	10.37	1.23
PT14_325'10''	99.31	4.95	-30.03	47.49	0.12	12.58	-0.85	0.01	11.58	10.36	0.81
PT14_326'4''	99.47	5.68	-30.36	52.06	0.13	12.49	-3.71	-4.22	10.69	9.16	0.77
PT14_326'8''	99.57	4.87	-29.84	43.85	0.13	12.31	-4.19	-4.84	14.82	12.16	0.74
PT14_327'4''	99.77	4.20	-29.34	45.12	0.11	7.28	-3.16	-4.03	2.30	4.12	1.62
PT14_327'7''	99.85	2.83	-29.53	42.38	0.08	6.24	-2.68	-0.67	5.01	5.14	0.93
PT14_328'4''	100.08	2.73	-29.44	41.79	0.08	6.35	-2.77	-0.62	12.44	12.48	0.91
PT14_329'4''	100.38	0.93	-30.33	19.22	0.06	6.74	-1.83	0.39	1.60	1.90	1.07
PT14_331'5''	101.02	1.29	-30.40	31.29	0.05	6.12	-1.98	0.85	3.23	3.52	0.98
PT14_332'8''	101.40	0.23	-27.48	6.68	0.04	4.73	-5.37	-4.19	1.04	4.09	3.55
PT14_335'7''	102.29	0.16	-26.94	3.79	0.05	3.76			0.79	0.56	0.64
PT14_337'10''	102.97	0.14	-26.65	3.94	0.04	4.05			0.78	0.58	0.67
PT14_338'8''	103.23	0.09	-26.52	4.42	0.02	3.33			0.52	0.50	0.88

Table 2: Iron speciation and pyrite sulfur isotope data. Ac. Fe = sodium acetate-soluble iron, Ox. Fe = ammonium oxalate-soluble iron, Dith. Fe = sodium dithionate-soluble iron, Py. Fe = pyrite-bound iron, Fe_T = total iron, Fe_{HR} = highly reactive iron.

Sample:	[m]	Ac. Fe [wt%]	Ox. Fe [wt%]	Dith. Fe [wt%]	Py. Fe [wt%]	Fe_T [wt%]	Fe_{Py}/Fe_{HR}	Fe_{HR}/Fe_T	$\delta^{34}S_{PY}$ [‰]
core C-128:									
C128_126.1	38.44	0.03	0.38	2.08	nd	nd	nd	nd	nd
C128_127.8	38.95	0.07	0.22	1.05	nd	nd	nd	nd	nd
C128_130.6	39.81	0.03	0.26	0.99	nd	nd	nd	nd	nd
C128_131.7	40.14	0.06	0.24	1.31	nd	nd	nd	nd	nd
C128_133.1	40.57	0.07	0.23	1.33	nd	nd	nd	nd	nd
C128_136.2	41.51	0.11	0.33	0.99	nd	nd	nd	nd	nd
C128_137.5	41.91	0.05	0.34	1.13	nd	nd	nd	nd	nd
C128_139.9	42.64	0.09	0.12	0.64	nd	nd	nd	nd	nd
C128_140.9	42.95	0.01	0.15	0.84	nd	nd	nd	nd	nd
C128_143.3	43.68	0.10	0.19	0.64	0.00	1.97	0.00	0.47	nd
C128_145.4	44.32	0.08	0.38	0.81	0.00	5.64	0.00	0.23	nd
C128_146.0	44.50	0.10	0.38	0.89	0.00	6.49	0.00	0.21	nd
C128_149.2	45.48	0.82	0.20	0.12	0.22	4.82	0.16	0.28	-5.72
C128_150.6	45.90	0.69	0.14	0.11	0.07	4.52	0.07	0.23	-7.39
C128_153.3	46.73	0.61	0.19	0.11	0.04	4.36	0.05	0.22	-13.21
C128_154.4	47.06	0.64	0.18	0.12	0.01	4.53	0.01	0.21	-11.97
C128_156.4	47.67	0.71	0.16	0.10	0.17	3.53	0.15	0.32	8.65
C128_157.9	48.13	0.51	0.12	0.12	0.40	4.66	0.35	0.25	-0.42
C128_160.3	48.86	0.64	0.09	0.09	0.52	4.45	0.39	0.30	0.32
C128_161.5	49.23	0.61	0.10	0.08	0.47	3.79	0.37	0.33	15.03
C128_162.4	49.50	0.40	0.07	0.07	1.30	4.19	0.71	0.44	12.60
C128_163.5	49.83	0.27	0.05	0.06	1.35	3.64	0.78	0.48	-5.56
C128_164.3	50.08	0.24	0.04	0.05	1.16	3.49	0.78	0.43	28.00
C128_165.2	50.35	0.38	0.05	0.05	0.70	2.87	0.59	0.41	34.69
C128_165.8	50.54	0.24	0.05	0.07	0.68	2.37	0.66	0.44	31.76
C128_166.2	50.66	0.18	0.10	0.09	0.63	2.93	0.63	0.34	46.78
C128_166.8	50.84	0.22	0.06	0.08	0.30	2.00	0.45	0.33	37.74
C128_167.7	51.11	0.07	0.03	0.04	0.95	2.86	0.86	0.38	4.41
C128_168.2	51.27	0.11	0.04	0.05	1.04	3.52	0.85	0.35	2.80
C128_168.5	51.36	0.16	0.04	0.04	1.08	3.04	0.82	0.43	-7.21
C128_169.1	51.54	0.28	0.03	0.04	0.77	2.92	0.68	0.39	-12.26
C128Tuff-6	51.64	0.43	0.03	0.04	0.47	1.71	0.48	0.57	-21.29
C128Tuff-5	51.66	0.31	0.03	0.04	0.94	2.22	0.71	0.60	-18.62
C128Tuff-4	51.66	0.92	0.16	0.22	6.57	7.80	0.84	1.01	-0.84
C128Tuff-3	51.67	0.39	0.04	0.04	0.47	1.51	0.50	0.62	-21.56
C128Tuff-2	51.68	0.50	0.04	0.04	0.89	1.72	0.61	0.85	-23.36
C128Tuff-1	51.69	0.52	0.03	0.04	0.92	1.87	0.61	0.80	-23.07
C128_169.8	51.76	0.22	0.03	0.04	1.03	2.83	0.78	0.46	-15.64

C128_172.6	52.61	0.11	0.05	0.06	1.92	4.94	0.90	0.43	6.45
C128_175.6	53.52	0.10	0.06	0.07	1.95	5.36	0.90	0.40	-7.07
C128_177.5	54.10	0.19	0.04	0.05	1.37	3.87	0.83	0.43	-11.41
C128_180.8	55.11	0.13	0.37	0.48	0.00	4.03	0.00	0.24	nd
C128_184.0	56.08	0.13	0.54	1.06	0.00	3.76	0.00	0.46	nd
C128_185.1	56.42	0.18	0.34	0.99	0.00	nd	0.00	nd	nd
C128_187.6	57.18	0.12	0.22	1.00	0.00	nd	0.00	nd	nd
C128_187.9	57.27	0.06	0.28	0.92	0.00	nd	0.00	nd	nd
C128_190.5	58.06	0.07	0.21	1.13	0.00	3.01	0.00	0.47	nd
core PT-14:									
PT14_296'0	90.22	0.10	0.49	1.32	0.00	nd	0.00	nd	nd
PT14_296'1	90.25	0.11	0.45	0.81	0.00	4.18	0.00	0.33	nd
PT14_297'5	90.65	0.10	0.47	1.01	0.00	5.44	0.00	0.29	nd
PT14_307'5	93.80	0.34	0.23	0.15	0.06	5.65	0.08	0.14	nd
PT14_311'1	94.82	0.52	0.15	0.11	0.20	4.70	0.20	0.21	-5.18
PT14_311'5	94.92	0.55	0.13	0.10	0.30	4.37	0.28	0.25	-4.05
PT14_313'7	95.58	0.92	0.30	0.13	0.05	4.40	0.04	0.32	-4.36
PT14_314'5	95.83	0.67	0.16	0.14	0.32	4.41	0.25	0.29	0.59
PT14_316'10	96.57	0.48	0.11	0.09	0.70	4.79	0.50	0.29	-4.80
PT14_318'5	97.05	0.79	0.12	0.11	0.48	4.25	0.32	0.35	11.61
PT14_321'6	97.89	0.31	0.05	0.04	1.07	4.22	0.73	0.35	-1.18
PT14_321'8	98.04	0.25	0.04	0.04	1.19	3.51	0.78	0.43	-5.62
PT14_323'1	98.48	0.17	0.05	0.06	1.21	4.34	0.82	0.34	-5.18
PT14_323'4	98.55	0.27	0.04	0.05	0.84	3.34	0.70	0.36	41.36
PT14_323'6	98.60	0.18	0.07	0.07	0.82	3.21	0.72	0.36	53.64
PT14_325'10	99.31	0.23	0.07	0.08	0.48	2.01	0.56	0.43	35.05
PT14_326'4	99.47	0.24	0.04	0.06	0.39	1.47	0.54	0.49	42.96
PT14_326'8	99.57	0.21	0.05	0.07	0.49	1.70	0.59	0.48	40.57
PT14_327'4	99.77	0.06	0.03	0.04	1.04	3.41	0.89	0.34	1.70
PT14_327'7	99.85	0.09	0.04	0.04	0.94	3.15	0.85	0.35	-11.84
PT14_328'4	100.08	0.19	0.03	0.04	0.73	2.45	0.74	0.40	-13.40
PT14_329'4	100.38	0.12	0.06	0.06	1.89	5.06	0.88	0.42	4.69
PT14_331'5	101.02	0.27	0.07	0.07	2.02	4.66	0.83	0.52	8.48
PT14_332'8	101.40	0.20	0.14	0.12	1.26	5.16	0.74	0.33	-13.09
PT14_335'7	102.29	0.24	0.41	0.15	0.00	5.86	0.00	0.14	nd
PT14_337'10	102.79	0.23	0.93	0.68	0.00	6.94	0.00	0.26	nd
PT14_337'3	102.97	0.20	1.11	0.45	0.00	6.32	0.00	0.28	nd
PT14_338'8	103.23	0.10	0.42	0.64	0.00	4.64	0.00	0.25	nd
PT14_343'7	104.72	0.19	0.77	0.76	nd	nd	nd	nd	nd
PT14_344'11	104.98	0.12	0.49	0.81	nd	nd	nd	nd	nd
PT14_344'5	105.13	0.13	0.75	1.06	nd	nd	nd	nd	nd
PT14_347'11	106.05	0.11	1.07	1.25	nd	nd	nd	nd	nd

Table 3: Elemental abundances.

sample ID	Pos. [m]	Na [%]	Mg [%]	Al [%]	P [ppm]	K [%]	Ca [%]	Ti [ppm]	V [ppm]	Cr [ppm]	Mn [ppm]	Fe [%]	Co [ppm]	Ni [ppm]	Cu [ppm]	Zn [ppm]	As [ppm]	Mo [ppm]	Cd [ppm]	U [ppm]
core C-128:																				
C128_143.3	43.68	2.88	0.68	5.73	370	1.69	4.53	2950	55	32	710	1.97	5.4	15.7	48.1	29.0	0.8	0.3	0.1	1.1
C128_145.4	44.32	2.00	2.50	7.79	460	2.74	1.77	4280	88	59	554	5.64	24.9	40.2	85.9	143.0	2.5	0.2	0.1	1.5
C128_146.0	44.50	1.21	2.84	8.35	560	3.25	1.40	4570	100	65	597	6.49	26.3	45.3	42.1	173.0	1.4	0.2	0.1	2.0
C128_149.2	45.48	1.39	3.74	7.83	392	2.96	4.05	3626	101	70	893	4.82	19.8	38.7	94.4	113.7	9.9	1.5	0.0	2.9
C128_150.6	45.90	1.40	3.25	8.61	120	3.25	2.61	3905	111	75	758	4.52	16.6	42.3	55.1	112.4	3.8	0.4	0.1	2.4
C128_153.3	46.73	1.42	2.74	7.91	486	2.94	2.28	4513	104	71	718	4.36	17.2	40.2	45.9	132.4	6.4	0.3	0.2	2.0
C128_154.4	47.06	1.25	3.10	7.60	438	2.90	2.89	4139	100	67	741	4.53	16.2	39.5	21.8	87.3	7.8	0.2	0.1	1.8
C128_156.4	47.67	1.45	2.01	6.68	489	2.39	2.90	4448	89	64	726	3.53	13.6	31.8	20.8	95.7	13.6	0.4	0.2	2.2
C128_157.9	48.13	1.34	3.32	8.54	329	3.50	2.61	4000	113	77	730	4.66	17.9	42.6	28.8	75.8	15.1	0.3	0.1	2.1
C128_160.3	48.86	1.10	3.34	7.88	344	3.40	3.12	4081	121	71	716	4.45	16.2	41.8	31.1	70.6	17.5	0.5	0.0	2.3
C128_161.5	49.23	1.00	2.81	6.90	370	3.18	3.00	4015	94	64	755	3.79	13.9	34.1	27.2	65.7	15.9	0.4	0.1	2.1
C128_162.4	49.50	0.94	3.02	7.03	331	3.33	2.88	3724	97	65	725	4.19	14.6	35.5	21.5	137.3	16.1	0.4	0.4	2.2
C128_163.5	49.83	0.67	3.56	6.67	235	4.07	4.10	3373	93	61	688	3.64	11.7	30.1	24.2	52.0	17.1	0.8	0.1	2.4
C128_164.3	50.08	0.69	3.33	6.22	306	3.38	3.33	3546	88	57	656	3.49	15.0	28.8	31.7	46.9	22.0	1.8	0.1	2.6
C128_165.2	50.35	1.26	5.53	5.59	183	2.04	6.09	2748	150	52	832	2.87	12.0	28.7	33.2	311.1	34.1	13.2	0.8	3.6
C128_165.8	50.54	0.62	5.49	4.13	192	1.58	4.69	2113	169	40	509	2.37	10.6	23.7	32.2	52.0	32.2	15.5	0.2	4.1
C128_166.2	50.66	0.31	6.82	4.77	202	1.82	4.80	2221	122	43	665	2.93	9.7	23.1	26.7	70.5	25.5	14.8	0.1	4.4
C128_166.8	50.84	0.30	7.40	3.23	170	1.27	5.50	1664	136	30	462	2.00	8.5	19.1	25.6	39.3	21.3	15.2	0.1	3.8
C128_167.7	51.11	0.53	5.24	5.49	298	2.10	2.66	2644	201	52	375	2.86	11.7	27.9	29.6	59.8	52.9	19.7	0.3	5.4
C128_168.2	51.27	0.85	4.04	6.71	321	2.44	2.20	3610	138	61	494	3.52	13.6	33.6	32.2	78.4	44.8	9.3	0.2	4.4
C128_168.5	51.36	0.86	4.02	5.98	243	2.21	2.68	2949	210	56	375	3.04	11.8	29.8	31.7	70.6	35.3	9.1	0.2	5.3
C128_169.1	51.54	1.18	4.38	5.73	273	2.04	5.33	2793	238	53	443	2.92	10.9	29.1	32.9	80.4	34.7	9.2	0.3	10.1
C128Tuff-6	51.642	0.73	7.93	2.78	165	0.87	12.77	2053	157	33	947	1.71	7.0	16.5	32.3	33.8	25.8	13.6	0.2	4.3
C128Tuff-5	51.656	0.82	6.81	3.32	196	1.15	11.02	2576	179	52	953	2.22	10.0	21.7	42.8	36.6	26.0	12.3	0.1	3.8
C128Tuff-4	51.664	3.93	0.91	5.63	334	0.31	4.98	4013	84	20	421	7.80	30.4	57.6	346.2	80.4	195.5	41.0	0.3	4.0

C128Tuff-3	51.670	0.52	8.10	2.22	1009	0.73	13.57	1777	149	39	1057	1.51	6.1	13.9	20.7	51.9	22.7	12.9	0.2	5.8
C128Tuff-2	51.678	0.88	7.79	2.92	162	0.89	12.76	2091	158	32	1009	1.72	6.8	15.9	21.3	30.6	26.9	14.1	0.1	3.0
C128Tuff-1	51.685	1.10	7.61	3.37	178	1.05	12.12	2258	171	35	987	1.87	8.1	19.2	27.3	66.6	32.4	16.2	0.1	2.7
C128_169.8	51.76	1.20	4.39	5.63	261	2.15	4.95	2759	236	52	473	2.83	11.6	29.1	31.6	68.3	29.5	11.1	0.3	7.7
C128_172.6	52.61	1.55	2.22	8.68	477	3.67	1.11	4011	119	81	632	4.94	18.0	44.0	37.3	102.8	21.8	2.6	0.1	4.3
C128_175.6	53.52	1.57	2.46	8.92	433	3.39	0.96	4224	123	83	630	5.36	18.8	45.0	40.3	91.9	22.0	2.7	0.1	3.6
C128_177.5	54.10	1.78	3.42	8.26	372	2.71	3.38	3768	192	76	911	3.87	17.8	40.6	52.2	295.9	41.4	16.6	0.9	3.0
C128_180.8	55.11	1.91	3.44	7.74	380	2.70	3.66	3970	189	76	857	4.03	16.4	36.4	45.2	310.0	39.2	16.6	0.9	3.1
C128_184.0	56.08	2.67	0.89	6.95	510	1.97	0.55	4450	90	60	265	3.76	14.5	35.2	17.8	60.0	1.6	0.1	0.0	2.1
C128_190.5	58.06	3.15	1.04	6.28	548	1.58	2.15	3617	71	55	1004	3.01	9.4	20.3	6.5	34.2	2.3	0.4	0.1	1.2
core PT-14:																				
PT14_296'1	90.25	2.44	1.99	8.09	490	3.12	2.13	4680	91	62	663	4.18	17.1	35.3	13.6	84.0	1.6	0.2	0.1	1.8
PT14_297'5	90.65	1.73	2.45	9.05	610	3.68	1.74	5030	120	83	678	5.44	25.9	57.3	18.2	119.0	3.0	0.3	0.1	2.5
PT14_307'5	93.80	1.57	3.13	8.43	505	2.82	1.21	5167	115	70	421	5.65	31.1	57.4	127.9	189.1	8.1	0.3	0.1	2.3
PT14_311'1	94.82	1.63	3.31	8.42	372	3.31	2.65	4085	110	74	675	4.70	17.3	40.7	44.6	114.8	7.8	1.3	0.1	2.4
PT14_311'5	94.92	1.66	2.73	7.84	437	2.90	2.45	4397	101	69	706	4.37	14.7	37.1	51.2	98.0	6.0	1.3	0.1	2.5
PT14_313'7	95.58	1.83	3.38	8.23	378	3.46	3.98	3796	107	75	950	4.40	13.7	35.2	21.6	76.6	7.0	0.3	0.0	2.4
PT14_314'5	95.83	1.68	3.27	8.08	358	3.40	3.34	3863	103	68	779	4.41	21.7	40.7	31.1	77.2	20.8	0.3	0.1	2.4
PT14_316'10	96.57	1.33	3.04	7.95	308	3.57	2.83	3938	122	73	753	4.79	17.5	42.2	35.1	67.6	18.6	0.4	0.0	2.4
PT14_318'5	97.05	1.17	3.01	7.83	374	3.61	3.39	4163	108	72	769	4.25	14.2	39.1	24.8	70.7	15.2	0.4	0.1	2.6
PT14_321'6	97.89	1.08	3.20	7.88	264	3.94	3.12	3999	121	73	684	4.22	12.1	38.2	26.2	58.5	14.0	0.3	0.1	2.2
PT14_321'8	98.04	0.72	3.64	6.53	265	3.93	4.05	3443	93	58	704	3.51	11.7	28.6	28.2	44.2	17.6	0.5	0.0	3.0
PT14_323'1	98.48	1.18	3.57	7.80	269	3.39	2.89	3835	111	71	649	4.34	13.2	37.1	28.6	54.5	14.9	0.5	0.0	3.0
PT14_323'4	98.55	1.62	5.03	6.38	185	2.30	6.10	3006	127	57	966	3.34	13.5	30.0	37.0	1050.5	24.1	3.8	4.5	3.3
PT14_323'6	98.60	0.84	5.50	5.77	239	2.16	4.69	2757	108	51	764	3.21	11.4	27.0	23.8	101.6	20.5	9.2	0.2	3.6
PT14_325'10	99.31	0.37	6.97	3.31	161	1.36	6.60	1629	131	31	596	2.01	8.0	18.1	22.5	41.4	28.6	16.5	0.2	3.2
PT14_326'4	99.47	0.46	5.40	2.54	142	1.05	5.90	1334	122	25	350	1.47	7.4	15.6	29.2	67.8	16.3	22.0	0.2	2.1
PT14_326'8	99.57	0.29	7.50	2.90	109	1.33	8.53	1519	133	28	488	1.70	7.9	16.6	22.6	38.1	19.1	11.5	0.2	1.9
PT14_327'4	99.77	0.98	4.15	6.62	267	2.48	2.54	3423	210	62	412	3.41	13.6	33.5	34.4	82.0	50.4	11.1	0.3	6.1
PT14_327'7	99.85	1.16	4.19	6.37	292	2.45	3.16	3245	251	61	424	3.15	12.9	32.9	36.1	89.9	37.0	13.9	0.3	9.2
PT14_328'4	100.08	0.86	5.95	4.56	231	1.72	7.69	2351	194	43	556	2.45	9.7	23.6	25.4	48.9	26.9	7.5	0.2	7.9

PT14_329'4	100.38	1.60	2.17	8.62	136	3.83	1.17	4329	119	79	785	5.06	19.6	46.5	37.7	99.0	24.7	2.0	0.3	4.7
PT14_331'5	101.02	2.21	2.42	8.61	451	3.71	2.30	3932	113	79	925	4.66	16.7	39.8	49.0	110.8	19.5	2.9	0.2	6.0
PT14_332'8	101.40	2.23	2.24	9.11	546	3.17	2.63	4156	123	81	915	5.16	26.3	45.4	43.5	68.8	54.2	0.6	0.0	5.6
PT14_335'7	102.29	1.53	2.54	9.92	536	3.23	0.48	4834	140	92	415	5.86	26.4	55.9	122.1	110.1	7.3	0.2	0.0	2.5
PT14_337'3	102.79	1.91	1.81	9.52	640	3.51	0.51	5020	141	89	418	6.32	24.0	55.1	12.8	102.0	2.6	0.3	0.0	2.6
PT14_337'10	102.97	1.50	2.18	9.76	640	3.72	0.43	5220	154	98	401	6.94	26.7	63.0	6.7	111.0	2.6	0.2	0.0	2.8
PT14_338'8	103.23	2.63	1.16	8.84	580	3.04	0.52	4800	119	75	362	4.64	15.9	40.9	8.6	71.0	1.8	0.2	0.0	2.3

Table 4: **Selected lipid biomarker parameters for rock extracts.**

position [m]	TOC [wt%]	H/S	C_{29} ααα St	%C_{30} Sterane	C_{30} βα	C_{30} diaH	2α-MeHI [%]	3β-MeHI [%]	Gam	Pr/Ph	Carotane
core C-128:											
45.48m	0.4	6.09	0.32	<0.01	0.31	0.03	10.49	7.91	6.23	bdl	bdl
48.13m	0.35	2.95	0.44	<0.01	0.15	0.33	10.32	5.92	25.25	0.90	bdl
48.86m	0.32	3.64	0.46	<0.01	0.08	0.43	8.79	4.24	12.18	n.m.	n.m.
49.83m	1.06	1.88	0.62	<0.01	0.07	0.44	3.83	5.23	3.23	0.61	5.07
50.08m	0.92	2.02	0.57	<0.01	0.07	0.42	3.66	5.22	3.33	0.49	6.03
50.35m	2.57	2.55	0.55	<0.01	0.08	0.32	2.58	5.46	2.35	0.79	3.60
50.84m	6.64	2.63	0.53	<0.01	0.11	0.33	2.14	4.77	2.58	0.74	29.93
51.54m	3.46	5.83	0.57	<0.01	0.07	0.24	5.60	2.95	1.08	0.72	0.55
52.61m	1.04	5.64	0.60	<0.01	0.07	0.24	6.63	3.11	1.04	0.58	1.61
core PT-14:											
98.04m	1.35	2.24	0.59	<0.01	0.08	0.47	3.9	4.76	2.89	0.66	2.51

TOC: total organic carbon
H/S: hopane/sterane ratio, C_{27}-C_{35} αβ- and βα-hopanes/ C_{27}-C_{30} ααα (R+S) and αββ (R+S) steranes
%C_{30} Sterane: absence of 24-n-propylcolestanes is indicative of a non-marine system
C_{29} ααα Str: C_{29} ααα Sterane (20S/20S+20R) ratio
C_{30} βα: C_{30} βα/(βα+αβ) hopane ratio
C_{30} diaH: diahopane ratio C_{30} diaH/C_{30} αβ-hopane ratio
2α-MeHI (%): 2α-methylhopane index, using the C_{33} homologues; C_{33} 2α-me (S+R)/[C_{33} 2α-me (S+R) + C_{32} αβ hopane (S+R)]*100
3β-MeHI (%): 3β-methylhopane index, using the C_{33} homologues to avoid co-elution of methylgammacerane at the C_{31} homologue; C_{33} 2α-me (S+R)/[C_{33} 2α-me (S+R) + C_{32} αβ hopane (S+R)]*100
Gam: Gammacerane index, [(gammacerane/(gammacerane + C_{30} αβ hopane)]*10
Pr/Ph: pristane/phytane
Carotane: ΣC_{40} carotanes/(*n*-C_{20}+*n*-C_{21})
n.m.: not measurable in full scan TIC traces due to low overall signal in organic-lean rocks